2012-04-26

Atomic Force Microscopy: Lateral-Force Calibration and Force-Curve Analysis

Evan V. Anderson
Worcester Polytechnic Institute

Atomic Force Microscopy: Lateral-Force Calibration and Force-Curve Analysis

by

Evan Vincent Anderson

A Thesis

Submitted to the Faculty

of the

WORCESTER POLYTECHNIC INSTITUTE

in partial fulfillment of the requirements for the

Degree of Master of Science

in

Nanophysics

May 2012

APPROVED:

x_____
Dr. Nancy Burnham, Advisor

x_____
Dr. Terri Camesano, Co-Advisor

x_____
Dr. Qi Wen, Master's Committee

x_____
Dr. Mingjiang Tao, Master's Committee

x_____
Dr. Germano Iannacchione, Department Head

Table of Contents

I – List of Tables and Figures

II – Abstract

This thesis reflects two advances in atomic force microscopy. The first half is a new lateral force calibration procedure, which, in contrast to existing procedures, is independent of sample and cantilever shape, simple, direct, and quick. The second half is a high-throughput method for processing, fitting, and analyzing force curves taken on *Pseudomonas aeruginosa* bacteria in an effort to inspire better care for statistics and increase measurement precision.

III – Acknowledgements

There were many people who helped reach this point; I just hope I can remember all whom I need to thank and find the words to show them as much appreciation as I feel and as they deserve:

- The students (former and present) who have had a significant input in my research, Rebecca Gaddis, Ivan Ivanov, and Paola Pinzon. It may have taken me even longer without them, and then I'd have no choice but to get my Ph.D. instead!
- The man who was generous enough to allow me to be a teaching assistant despite my pursuit of a Master's Degree, Dr. Padmanabhan Aravind. Without him, I'd either only have a Bachelor's Degree, or I'd be drowning in debt!
- My Thesis Committee members, Dr. Mingjiang Tao and Dr. Qi Wen, whom I hope to not incite with regret for agreeing to be a part of this process. Thank you for taking the time to help me through this final stage of my degree.
- My co-advisor, Dr. Terri Camesano, who was a great mentor as well as an incredible biology and chemistry translator for both Nancy and for me. It was very rewarding to work across disciplines with you and learn things that would have evaded me entirely if I were locked up in the basement of Olin Hall. You were always very kind and understanding having seen others encounter the same obstacles I did, and you were always able to inspire me to continue and try things differently. I surely would not have made it this far without you.

and last, but certainly not least,

- My primary advisor, Dr. Nancy Burnham, who taught me everything I know about AFM and possibly even more so about the frustrations of experimental research. When my research was most fruitless, you helped me to see and even experience the results of hard work and determination—which became Chapter 2 of this thesis and published in *ACS Applied Materials and Interfaces*. I still prefer thinking of bacteria as bugs, and 'bughair' is much easier to say than 'lipopolysaccharides.' I can't thank you enough for your patience, your guidance, and most importantly, how well prepared I now feel for a career in Nanotechnology.

1. Introduction

Contained in this thesis are two manuscripts that have been submitted for publication in different journals. This thesis is meant to demonstrate research in two different aspects of atomic force microscopy, calibration and analysis. The first manuscript is a project on lateral force calibration; the second involves force-curve analysis on bacterial 'hairs.' This introduction will provide a brief background of atomic force microscopy, lateral force microscopy, biofilms, force curves, and modeling.

1.1 AFM Background

Scanning probe microscopy (SPM) is a unique discipline of microscopy where the resolution of the microscope is not limited by wave diffraction (as in optical and electron microscopes). This is attributed to the use of a probe used to make observations of the sample instead of light or electrons. Atomic force microscopy (AFM) is a type of scanning probe microscopy where the probe can be used to physically contact the substrate to obtain topographical information as well as material properties. The resolution of an atomic force microscope is limited primarily by the radius of the tip of the cantilever (collectively known as probe), the sensitivity of the detection system, cantilever spring constant, and noise.

AFM works by monitoring the deflection of the cantilever as it scans across a sample. The deflection is recorded by reflecting a laser off the back of the cantilever and into a position-sensitive photodiode as shown in Figure 1.1. The probe or sample stage is

typically driven by a piezoelectric material whose morphology is affected by electric fields. This property is manipulated to cause small and precise movements of the probe.

The ability to move the probe with precision and speed allows for an important feature of SPM known as the feedback loop. A feedback loop is used to keep something constant. For instance, cruise control in an automobile is regulated by a feedback loop. It acts to keep the car at a constant speed while traversing up- or downgrades in the road; the engine works harder in order to keep the car at a constant speed while moving up a hill, while the brakes may be applied while going downhill. In the case of SPM or AFM, feedback loops are employed to keep constant: force, distance, current, amplitude, etc. These imaging modes each have advantages for different purposes.

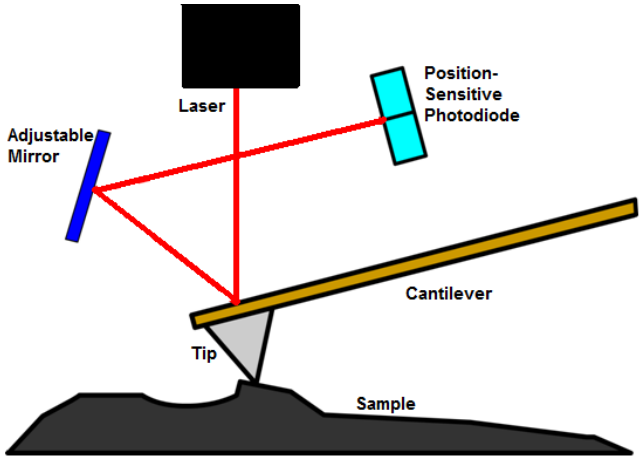

Figure 1.1 – A schematic for the instrumental setup for an AFM.

1.2 Lateral Force Microscopy

Lateral force microscopy (LFM) is a technique within AFM in which the lateral displacement and twisting of the cantilever are monitored (simultaneously with the

deflection) as seen in Figure 1.2 (left). It is primarily used for qualitative friction studies at the micro and nanoscales and is consequently also commonly known as friction force microscopy. LFM has been used to diagnose and optimize MEMS and NEMS (micro- and nano- electrical mechanical systems), determine adhesion strength of bacteria and nanoparticles, and even to determine the effectiveness of hair conditioner [1-6].

A persistent problem in LFM is the difficulty of making quantitative measurements. This stems from the complexity of calibrating a cantilever's lateral spring constant. A large scientific effort has been dedicated to develop more efficient calibration methods. Despite this effort, there are still several problems with the existing approaches: they often require expensive or specialized samples or equipment, are time-intensive, difficult to perform, calibrate a cantilever other than the one to be used, are incorrect, and can cause damage to the probe. There is still no widely-accepted calibration method [6-10].

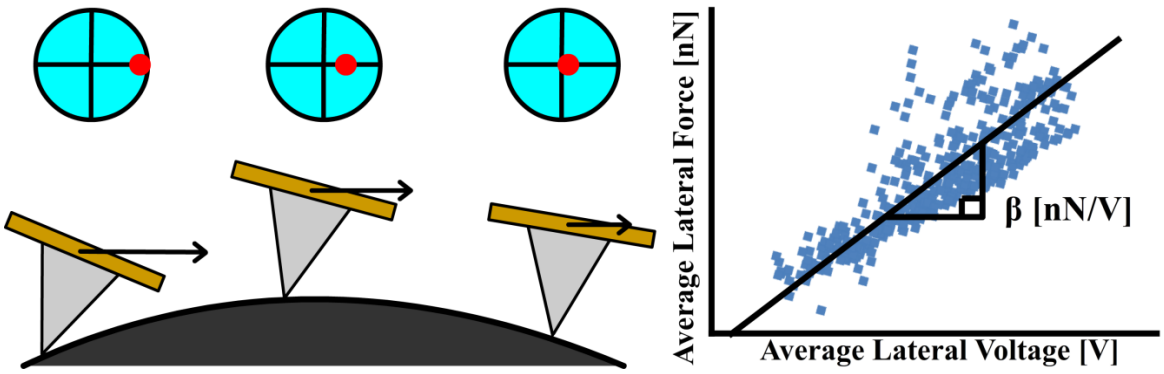

Figure 1.2 – The movement of the laser on the photodiode is dependent on the lateral force experienced by the cantilever as it scans across a surface (left). The lateral voltage read by the photodiode is linearly dependent on the lateral force on the probe, allowing for a least-squares fit to obtain a conversion factor between lateral force and voltage (right).

1.2.1 A New Calibration Procedure

Chapter 2 is a detailed account of the approach, execution, and validation of a new lateral force calibration method which was found to be independent of both sample and cantilever geometry. This work was published in *ACS AMI*, along with Appendix I – Supporting Information for Chapter 2 [11]. The basis of this technique is that a conversion factor can be obtained that relates the quantitative lateral force to the qualitative lateral voltage. The approach was to: model the forces on the cantilever as it scanned across a generic sample, assume equilibrium, solve Newton's Second Law for the average lateral force, plot lateral force (from theory) as a function of average lateral voltage from experiment (see Figure 2), and obtain the slope of the line that best fits the data, the calibration factor, by Equation 1.1.

$$\bar{F}_{lat} = \beta \bar{V}_{LFM} + \gamma, \tag{1.1}$$

where $\bar{F}_{lat}$ is the average lateral force, β is calibration factor, $\bar{V}_{LFM}$ is the average lateral voltage, and γ is the calibration intercept.

After modeling the forces on the cantilever, there are seven forces and only three equations (one for each direction). In order to solve for the lateral force, four variables must be either measured or neglected. Newton's Second Law for the *i*-*j*-*k* directions are:

$$\sum F_i = F_{lat} + O \sin\alpha \sin\theta - (N - A)\cos\alpha \sin\theta \mp \mu(N + A)\cos\theta = 0, \tag{1.2}$$

$$\sum F_j = F_{load} \sin\varphi - O\cos\alpha - (N - A)\sin\alpha + F_{axis}\cos\varphi = 0, \tag{1.3}$$

$$\sum F_k = -F_{load}\cos\varphi - O\sin\alpha\cos\theta + (N - A)\cos\alpha\cos\theta \mp \mu(N + A)\sin\theta + F_{axis}\sin\varphi = 0. \tag{1.4}$$

Here F_{lat} is the lateral force, F_{load} is the load force, F_{axis} is the force along the axis of the cantilever, φ is the cantilever angle of repose (the angle the cantilever makes with the scan head), O is the force in the plane of the sample, N is the normal force, A is the adhesion force, μ is the coefficient of friction, and α and θ are the angles of the sample. Amontons' First Law was chosen to describe the friction, $f = \mu(N + A)$. The $\mp$ signs denote the difference in direction for forward and reverse scans. Figure 1.3 depicts these forces.

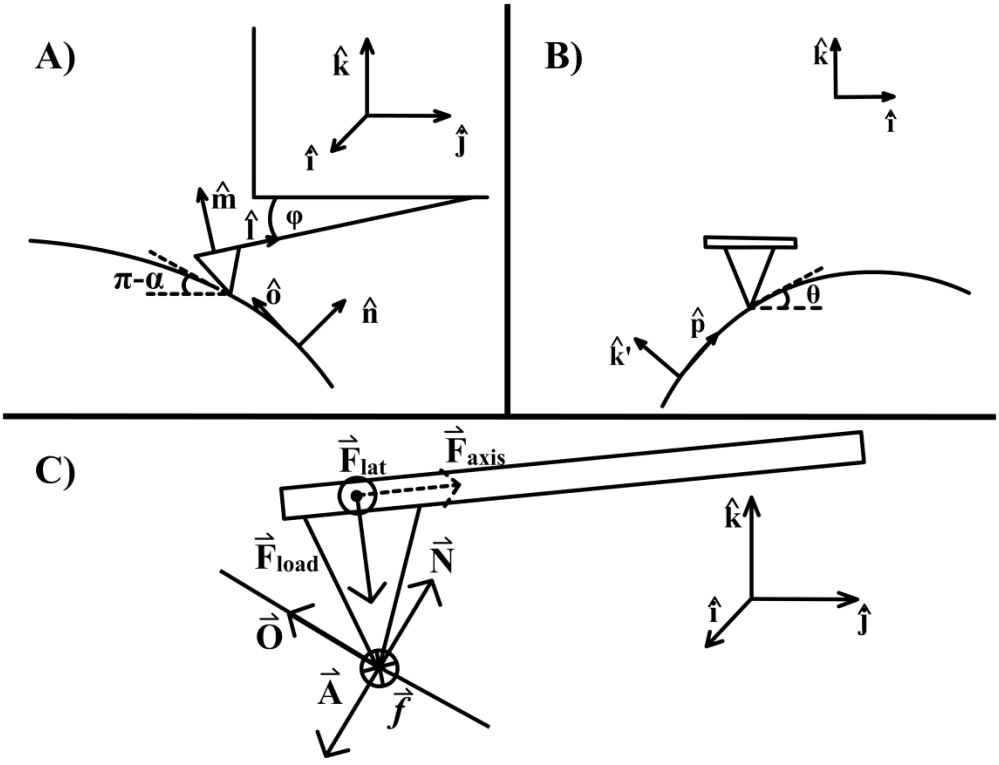

Figure 1.3 – The forces acting on the tip as it scans across a generic sample. The definitions of the forces are given in the paragraph above.

Adhesion and the load force are easily measured, leaving five forces and three equations. Friction is averaged out, leaving four variables. The orthogonal force is usually

neglected in the literature, but here the axial force is shown to be negligible—an insight previously unseen. The result for the average lateral force is shown in Equation 1.5.

$$\bar{F}_{lat} = F_{load} \cos\varphi \tan\theta \left[\frac{1+\mu^2 \cos^2\alpha(1+\tan\alpha\tan\varphi\sec\theta)}{1-(\mu\cos\alpha\tan\theta)^2}\right] + 2A\left[\frac{\mu^2\cos\alpha\tan\theta\sec\theta}{1-(\mu\cos\alpha\tan\theta)^2}\right]. \quad (1.5)$$

The theoretical average lateral force can now be determined for an image based on the measured quantities: load force, adhesion, and sample angles (the appearance of μ is more involved and will be saved for Chapter 2). More conveniently, the sample angles are calculated directly from the slopes of the topography images at each point.

The experimental portion of Chapter 2 includes different "stress tests" of this calibration technique, including the calibration factor's dependence on: load force, scan rate, gain, sample wear, sample topography, and tip geometry. While proven successful, there are still several improvements and investigations to be done in the future to increase the integrity of this procedure. Its simplicity, speed, and universality are our primary contributions. This method requires only one set of images (forward and reverse topography and lateral force) to obtain a calibration factor, thereby alleviating many of the persistent problems of existing procedures while maintaining similar or better accuracy and precision.

1.3 Biofilms, Bacteria, and Force Curves

The project in Chapter 3 focuses on the modeling and interpretation of force curves taken on bacteria. Understanding the forces that aid bacteria in adhering to surfaces is paramount to the prevention of biofilm formation. Biofilms are colonies of microorganisms that can cause a lot of problems if they form in the wrong place. Biofilms are responsible for

65% of infections in the Western Hemisphere [12]. They constitute over half of the Earth's biomass, and 99% of bacteria reside in biofilms [13]. This presents a problem because antibiotics are typically developed to combat planktonic or individual bacteria, but biofilms are resistant to doses of up to one-thousand times of what would kill an equal amount of planktonic cells [13]. There is no completely effective way to remove a biofilm, and for this reason it is important to attempt to prevent their formation altogether.

Biofilms' formation begins with the attachment of a single bacterium to a substrate. That bacterium then secretes sugars that assist other bacteria and microorganisms to adsorb to the surface as well [12-14]. Once a significant amount of bacteria have accumulated, they begin to build up and away from the substrate to form mushroom-like structures which allow nutrients to flow within the biofilm matrix. The bacteria are able to perceive the viability of this stage through a phenomenon known as quorum sensing [13]. The final stage of biofilm formation is also made possible through quorum sensing. At a sufficient concentration, pieces of the hierarchal structures break off to colonize new areas or surfaces.

1.3.1 Force Models

AFM has become a principle tool in the investigation of bacterial adhesion forces via the ability to probe mechanical characteristics of microscopic (and nanoscopic) subjects. The AFM records the forces encountered during the approach, contact, and retraction from a surface. Considerable research has been devoted to understanding the retraction portion of force curves, typically the maximum adhesion measured, in order to determine the

conditions that most inhibit adhesion and therefore reduce the chance of biofilm formation[15, 16]. A smaller, yet substantial effort attempts to formulate a mathematical model to predict and describe the approach portion of the force curve. Many such models have been proposed and tested, and are not necessarily limited to bacteria or even AFM.

The origin of the model found in Chapter 3 is based on the theoretical pressure experienced between two polymer-grafted plates (Figure 1.4). S. Alexander and P. de Gennes described this pressure by Equation 1.6,

$$P = \frac{k_B T}{s^3}\left[\left(\frac{2L_0}{D}\right)^{9/4} - \left(\frac{D}{2L_0}\right)^{3/4}\right], \tag{1.6}$$

where k_B is Boltzmann's constant, T is temperature, s is the "grafting density," L_0 is the equilibrium brush thickness, and D is the distance between the plates [17]. The first term is related to the osmotic pressure of the brush and the second is a result of the elasticity of the polymers [17]. Any model derived from or related to this one is known as AdG (Alexander-deGennes) theory.

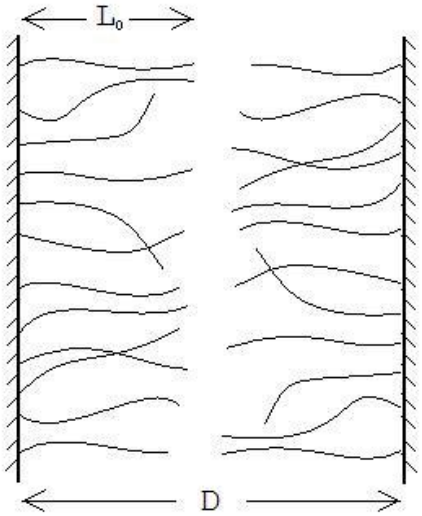

Figure 1.4 – A depiction of the experiments conducted with the surface forces apparatus by S. Alexander and P. deGennes.

Many have adapted AdG theory for AFM tip geometries, the most popular of which is a sphere [15, 18-24]. This can be done by integrating the pressure over the cross-sectional area of the tip, resulting in an equation for force as a function of distance (sphere-flat geometry). The model can also be converted to describe the force between a bare tip and a polymer-covered surface by substituting L for $2L_0$. Although many have arrived at different pre-factors, the form of the result generally agrees with Equation 1.7,

$$F_{spherical} = \frac{8\pi k_B T R L}{35 s^3}\left[7\left(\frac{L}{D}\right)^{5/4} + 5\left(\frac{D}{L}\right)^{7/4} - 12\right], \quad (1.7)$$

where R is the tip radius, d is the separation, and h is related to the compressibility of the polymer brush (essentially the distance at which the tip can no longer compress the brush). We also derived formulae for alternative tip geometries using the same method. Equations 1.8 and 1.9 are the result of conical and pyramidal geometries, respectively:

$$F_{conical} = \frac{32\pi k_B T L^2}{385 s^3} \tan^2\theta \left[77\left(\frac{L}{D}\right)^{1/4} + 33\frac{D}{L} - 5\left(\frac{D}{L}\right)^{11/4} - 105\right], \quad (1.8)$$

and,

$$F_{pyramidal} = \frac{128 k_B T L^2}{385 s^3} \tan^2\theta \left[77\left(\frac{L}{D}\right)^{1/4} + 33\frac{D}{L} - 5\left(\frac{D}{L}\right)^{11/4} - 105\right], \quad (1.9)$$

where θ is the half angle of the cone or pyramid. It is worth noting that this is the first time these geometries have been considered in the literature. These models are only applicable to a particular region of the force curve as described in Chapter 3; the raw data must be cropped before fitting a force model.

1.3.2 The Motive and Objective for Research

The objective of Chapter 3 was to determine the physical meaning of the parameter s, an ambiguous parameter originally deemed the grafting density, but taken by many to represent the root spacing between polymers [18-20]. We hypothesize that s is actually the mesh spacing, or distance between entangled points in the polymer brush—a conclusion reached via thought experiment. It seems more logical that the force be dependent on a three-dimensional density parameter as opposed to a two-dimensional density because the tip has no interaction with the roots of the polymers, only the heads. The mesh spacing of the polymers, could, of course, have some functional relation to their root spacing.

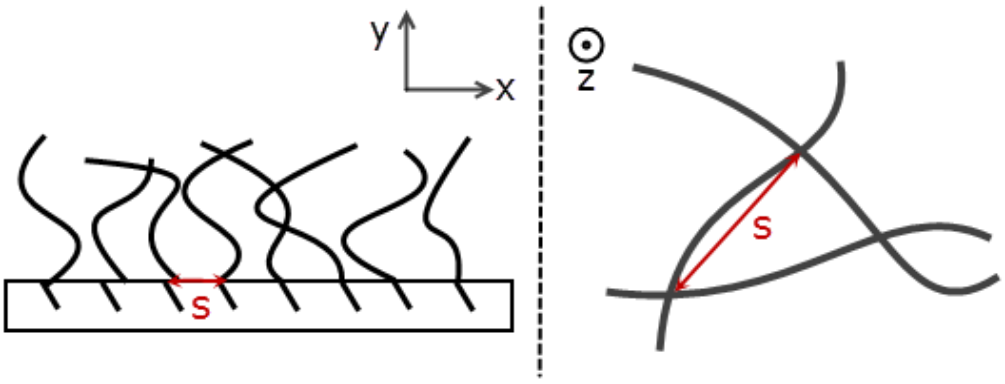

Figure 1.5 – A) The root-spacing interpretation of *s* and B) the mesh-spacing interpretation of *s*.

In order to determine which interpretation of *s* is correct, the conformation of the polymer brush must be manipulated. The bacterium *Pseudomonas aeruginosa* was chosen as the subject for investigation instead of a synthetic polymer brush because of its relevance to biofilm research. Research has shown that most bacterial polymers, such as lipopolysaccharides (LPS), react to changes in ionic strength and pH in solution. The LPS will extend in higher pH and ionic strength because the charged groups present in the individual polymers repel one another, causing them to equilibrate at a lesser density. The charges in these polymers are less apparent at lower pH and ionic strength and the LPS have less aversion to close proximity. We theorize that the LPS would equilibrate at much different conformations in reaction to extreme pH changes; the LPS would be dense and highly-entangled at low pH, and sparsely-entangled at high pH. Therefore, the mesh spacing would certainly change if the pH was varied while the root spacing should remain the same.

The experiment was designed to take force curves on bacteria under different pH conditions, fit the experimental data with the appropriate AdG force model, extrapolate the three fitting parameters (L, s, and h), and observe the trends in each as a function of pH. The predictions based on current literature were that L, the mean brush thickness, and s, the root or mesh spacing, would increase with pH.

1.3.3 Emphasis on Data Handling and Analysis

Due to the high cell-to-cell variability in bacteria, large quantities of force curves need to be acquired to accumulate statistics concerning surface properties. This presents a problem because it can be time consuming to process, fit, and analyze several force curves. This has driven some researchers to take shortcuts which may be detrimental to the quality of their results [21, 23, 25, 26].

The focus of the research detailed in Chapter 3 was shifted towards proper cropping and efficient treatment of force curves as a consequence of the ambiguous results concerning s. A significant effort was directed towards reducing error bars in order to show trends for L and s which resulted in the acquisition of large quantities of force curves in each pH condition. The force curves were originally manually-cropped and fit to the force model at a rate of nearly one curve per minute. With an average of one thousand curves per experiment, it was unfeasible to analyze every curve. We also found that the fitting results were extremely sensitive to how they were cropped. This posed an even larger problem than the time efficiency because the only method of cropping was subject to human error and judgment.

Matlab was used in an attempt to remove human subjectivity and increase time efficiency for force curve processing, fitting, and analysis. A program was written to mathematically crop large quantities of force curves so only the regions in which the force model was valid remained. The program then fits these force curves to the appropriate model and saves the results of the fits. In an effort to reduce error bars, the standard deviation of the mean and Chauvenet's Criterion are applied. The standard deviation of the mean is defined as $\sigma_{\bar{x}} = {}^{\sigma_x}/_{\sqrt{N}}$. Chauvenet's Criterion is an objective method to remove outliers—if the probability of obtaining the datum in question multiplied by the number of data points is less than one half ($P(x)N < 1/2$), it may be discarded.

Although the original question regarding the true meaning of s is still unclear, the implementation of this program removes subjectivity and greatly increases time efficiency for force-curve analysis, and will hopefully remove some of the aversion to handling large data sets. This can also assist future students who seek to determine the meaning of s with a different experimental approach. A manuscript based on Chapter 3 will soon be submitted to *Ultramicroscopy*.

2. Shape-Independent Lateral Force Calibration

2.1 Introduction

Also known as friction force microscopy, lateral force microscopy (LFM) is a technique used to make friction measurements on the micro- and nano-scales. Instead of observing topography with the vertical deflection of the cantilever as in traditional atomic force microscopy (AFM), the lateral deflection or twisting of the cantilever is observed. The lateral force on the cantilever provides information about the friction between the tip and sample.

LFM has been the key to experimental and theoretical developments in tribology and a wide variety of applications in chemistry, physics, and biotechnology on the nanoscale [27-31]. Cantilevers with low lateral spring constants can provide friction resolution as high as 10 picoNewtons, which is roughly the force required to 'unzip' DNA [7, 32]. LFM has been used to measure lateral bonding strength by functionalizing the tip with one chemical and the surface with another, and to investigate the critical shear force needed to dislodge bacteria such as *Staphylococcus aureus* and *Pseudomonas aeruginosa* [1, 2, 33, 34]. LFM is being applied to systems where friction must be minimized, such as microelectromechanical systems (MEMS) and nanoelectromechanical systems (NEMS), and to more novel applications such as the characterization of damaged and conditioned human hair [3, 5, 6, 35].

The primary problem with LFM has been the difficulty in calibrating the cantilever and tip in order to obtain quantitative data; researchers have often been limited to qualitative relative comparisons. Several review and research articles have expressed this difficulty and the need for a simple, universally-accepted method [6-10]. A quick and simple quantitative approach would enable the comparison of nano- and macro-scale friction studies.

The available procedures have numerous limitations. Some require specialized samples or setups [36-40]. Others are difficult to perform [41-44]. A number of them are indirect, or only suitable for certain cantilevers [38, 41-43, 45]. Several risk damage to the tip or sample, or both, and might require the geometry of the cantilever, which can be time-consuming to measure [40, 44, 46, 47].

2.2 Our Calibration Procedure

Proposed here is a new calibration technique that alleviates the aforementioned problems. It is independent of the shape of the sample and cantilever, requires only one set of images (minimizing tip wear and calibration time), is independent of scan parameters including load force, scan rate, and gain, and its precision is better than 10%. The entire calibration process can be as fast as fifteen minutes depending on the instrument, and a majority of this time is spent calibrating the normal (perpendicular to the plane of the cantilever) spring constant.

The construction of our model begins by relating the coordinate axes of the cantilever and arbitrarily-shaped sample to that of the scanner. If the axes of the scanner are *i*-*j*-*k* (Figure 1.1A) and the cantilever is in the *j*-*k* plane, the cantilever axes are obtained by rotating through an angle φ about the *i* axis. Similarly, the axes of the sample are obtained by first rotating through an angle θ about the –*j* axis to obtain *k'* (an intermediate transformation axis) and *p* (Figure 2.1B) and then rotating through an angle α about +*p* to obtain *n* and *o* (Figure 2.1A). These rotations are all counterclockwise. This gives the following set of unit vectors: *i*, the fast-scan direction of the scanner, *j*, the slow-scan direction of the scanner, *k*, the vertical axis of the scanner, *l*, the direction of the cantilever long-axis, *m*, the direction normal to the cantilever, *n,* the direction normal to the sample, *p*, the direction of the path of the tip in the plane of the sample in the *i*-*k* plane, and *o*, the direction mutually orthogonal to *n* and *p*. The relations between these vectors and the scanner axes are shown in Equations 2.1-2.5.

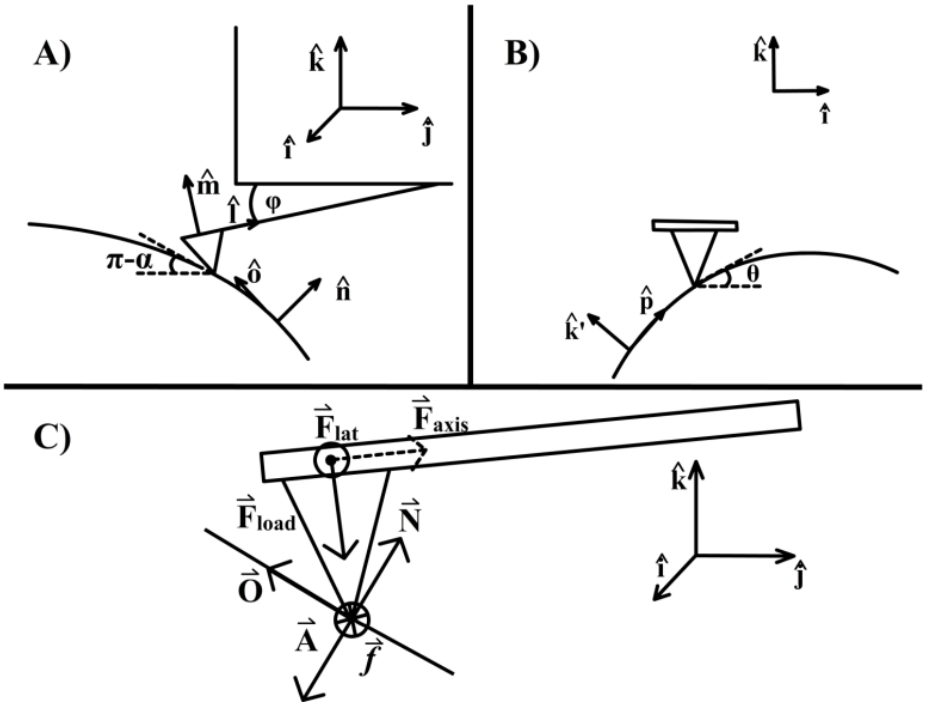

Figure 2.1 – This diagram illustrates the coordinates and forces involved in the model. A) Fast-scan perspective with scanner (*i,j,k*), cantilever (*l,m*), and sample axes (*n,o*) in the *j-k* plane. B) Slow-scan perspective showing the sample axis, *p*, and intermediate axis, *k'*, in the *i-k* plane. C) Free-body diagram depicting the forces on the cantilever tip. The definitions of the forces are given in the text.

$$\hat{l} = \cos\varphi\,\hat{\jmath} + \sin\varphi\,\hat{k}. \tag{2.1}$$

$$\hat{m} = -\sin\varphi\,\hat{\jmath} + \cos\varphi\,\hat{k}. \tag{2.2}$$

$$\hat{n} = -\cos\alpha\sin\theta\,\hat{\imath} - \sin\alpha\,\hat{\jmath} + \cos\alpha\cos\theta\,\hat{k}. \tag{2.3}$$

$$\hat{o} = \sin\alpha\sin\theta\,\hat{\imath} - \cos\alpha\,\hat{\jmath} - \sin\alpha\cos\theta\,\hat{k}. \tag{2.4}$$

$$\hat{p} = \cos\theta\,\hat{\imath} + \sin\theta\,\hat{k}. \tag{2.5}$$

Amontons' Law is assumed for friction; the force of friction is proportional to the sum of the normal force and adhesion, as seen in Equation 2.6.

$$f = \mu(N + A). \tag{2.6}$$

Although future versions of this model could accommodate alternative friction laws, this assumption often holds at the nanoscale [48].

The next step is to sum the forces in i, j, and k directions and impose equilibrium conditions. The free-body diagram of the forces on the tip can be seen in Figure 2.1C. Only three variables may be solved for because there are only three equilibrium equations. The equilibrium equations for the *i-j-k* directions are:

$$\sum F_i = F_{lat} + O \sin\alpha \sin\theta - (N - A)\cos\alpha \sin\theta \mp \mu(N + A)\cos\theta = 0, \tag{2.7}$$

$$\sum F_j = F_{load} \sin\varphi - O\cos\alpha - (N - A)\sin\alpha + F_{axial}\cos\varphi = 0, \tag{2.8}$$

$$\sum F_k = -F_{load}\cos\varphi - O\sin\alpha\cos\theta + (N - A)\cos\alpha\cos\theta \mp \mu(N + A)\sin\theta + F_{axial}\sin\varphi = 0. \tag{2.9}$$

Here F_{lat} is the lateral force, F_{load} is the load force, F_{axial} is the force along the axis of the cantilever, φ is the cantilever angle of repose, O is the force in the o direction, N is the normal force, A is the adhesion force, μ is the coefficient of friction, and α and θ are the sample angles. Using these equations, the lateral force in the forward (+) and reverse (-) directions can be solved for, as shown in Equation 2.10.

$$F_{lat\pm} = \frac{F_{load}}{(1 \mp \mu\cos\alpha\tan\theta)}\left[\cos\varphi\tan\theta \pm \mu\left(\cos\alpha\cos\varphi + \sin\alpha\sin\varphi\sec\theta\right)\right] \pm \frac{2\mu A\sec\theta}{(1 \mp \mu\cos\alpha\tan\theta)} - \frac{F_{axial}}{(1 \mp \mu\cos\alpha\tan\theta)}\left[2\tan\alpha\cos\varphi\sin\theta + \sin\varphi\tan\theta \pm \mu\cos\theta\left(\sin\alpha\cos\varphi + \cos\alpha\sin\varphi\sec\theta\right)\right] \tag{2.10}$$

The axial term is small because it contains the small angles α and φ and because the fast-scan direction is orthogonal to the long axis of the cantilever; the axial term is therefore subsequently neglected.

For comparison with earlier work, if the angle of repose, φ, and the angle of the sample in the y-direction, α, are also set to zero, Eqs. 2.5 and 2.6 of Varenberg are almost recovered [38]. There is a small difference (a factor of two) in the adhesion term; this stems from the difference in assumptions of the friction law. In Varenberg's paper, friction force was $f = \mu N$; here it is $f = \mu(N+A)$. The discrepancy is small, as in both cases the term is multiplied by μ. Yet by allowing α and φ to be nonzero and the subsequent necessity of including the orthogonal force O, the more general case is developed here. Furthermore, the axial term has not been previously treated.

Continuing on, the average and difference between the lateral force from forward and reverse scans are shown in Equations 2.11 and 2.12 respectively.

$$\bar{F}_{lat} = F_{load}\cos\varphi\tan\theta\left[\frac{1+\mu^2\cos^2\alpha(1+\tan\alpha\tan\varphi\sec\theta)}{1-(\mu\cos\alpha\tan\theta)^2}\right] + 2A\left[\frac{\mu^2\cos\alpha\tan\theta\sec\theta}{1-(\mu\cos\alpha\tan\theta)^2}\right]. \quad (2.11)$$

$$\Delta F_{lat} = \frac{2\mu}{\cos\theta}\left[\frac{F_{load}\cos\varphi\cos\alpha(\sec\theta+\tan\varphi\tan\alpha)+2A}{1-(\mu\cos\alpha\tan\theta)^2}\right]. \quad (2.12)$$

Equation 2.11 is the primary equation of interest because it is used to find the calibration factor, β, and intercept, γ, using the linear relationship between the average lateral force, $\bar{F}_{lat}$, and the average lateral voltage, $\bar{V}_{LFM}$, as shown in Equation 2.13.

$$\bar{F}_{lat} = \beta\bar{V}_{LFM} + \gamma. \quad (2.13)$$

Use of a sample with a large range of angles will yield a more accurate calibration factor because of the wider range of data used to find the slope in the force-voltage plot.

Our calibration program (described on page 55) implements Equations 2.11 and 2.12. It requires the measurement of the normal spring constant, z-scanner displacement, and average adhesion. The normal spring constant was calibrated by using the resonance frequency of the cantilever from a thermal spectrum as described by Matei et al [49]. The average adhesion between the tip and sample was found by acquiring 16 force curves along the apex of a pulled micropipette, equally-spaced along the length of the image.

Pulled micropipettes are recommended as samples for their ease of use, availability, low cost, and wide range of sample angles. They are also easily made from normal micropipettes by heating the center and pulling the ends apart. The pipettes are placed in the AFM with their long axes perpendicular to the fast-scan direction, which is orthogonal to the long axis of the cantilever. If larger sample angles are desired, one moves down the pipette; if the angles are too steep for stable imaging, one moves up the pipette. Although a pipette is convenient, any sample with at least two slopes may be used, unlike earlier work in which the shape of a sample with known slope(s) is prescribed [38, 39, 45].

2.3 Experimental Validation

Each experiment was performed in a similar fashion by using a pyramid-type variation of parameters. For example, the set point of the force was varied from 0 to -7 Volts in increments of 1 Volt, and then back down to 0 in the same manner until three data

points had been acquired for each set point. The scan rate and gain were varied the same way until four data points were collected. A set point of -5 Volts was typical for these experiments. The effect of sample wear was tested by allowing the AFM to scan for 70 minutes, resulting in 16 sets of images and consequently 16 calibration factors. To investigate the influence of sample shape, two areas on the micropipette were imaged that had drastically different radii of curvature. Five sets of images were taken at each radius. More experimental details are given in the supplement.

Figure 2.2A-D shows a typical set of images (forward and reverse topography and LFM) of a pulled micropipette. Figure 2.2E shows an example calibration plot (LFM voltage on the x-axis, Equation 2.11 on the y-axis) which gives the calibration factor, β, and the intercept, γ, needed to convert the lateral signal from Volts to nanoNewtons (Equation 2.13).

There were several things to test to ensure the validity of this technique including the calibration factor's dependence on: the shape of the sample and cantilever, load force, scan rate, gain, repeatability, precision, and accuracy. The calibration factor should be independent of the scan parameters, be repeatable, and have good precision and accuracy. On average, the calibration factor varied by about 7% between images taken on the same sample. The accuracy of the calibration was tested at an order-of-magnitude level by comparing lateral spring constants found experimentally with those found geometrically (see Calibration Accuracy section of Appendix I – Supporting Information for Chapter 2). They were within 65% of each other.

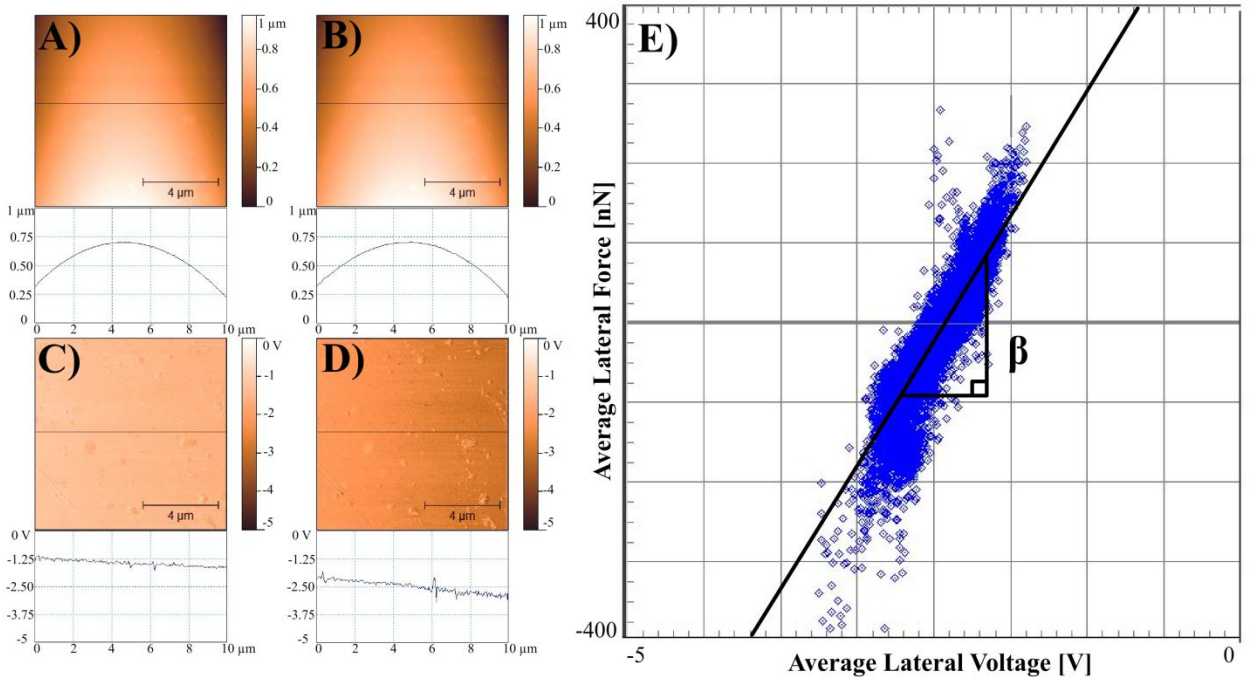

Figure 2.2 – A typical set of images, cross-sections across the middles of the images, and a calibration plot are shown for a pulled micropipette. A) Forward and B) reverse topography, for which the angle in the i-k plane ranges from +9° to -10°. C) Forward and D) reverse lateral force in volts, where the cross-sections are linear because the response is dominated by the first term in Equation 10, which is linear for the range of angles in A) and B). E) A plot of the average lateral force in nanoNewtons against the average lateral voltage in Volts for the 65,536 datum points; the slope of the straight-line fit is the calibration factor β. The calibration factor and intercept can then be used to convert the lateral force voltage into a quantitative force. The calibration factor and intercept for this example are 256 nN/V and 624 -nN respectively.

The calibration factor was assumed to be independent of sample topography because the lateral force is calculated based on the measured slopes of the sample. Theoretical test files were generated that model the topography and lateral voltage signal of a cone and a sphere. When run through the calibration program, these files produced a perfectly linear plot of lateral force against lateral voltage; the calibration factors were the same. This assumption was also tested by imaging a pulled-micropipette at two different radii of curvature—the larger of which had very rough topography—and the calibration factor was statistically equivalent, as seen in Figure 2.3. Although the two different sets of images are

from the same sample, the topography was different enough to conclude that the calibration factor was independent of sample shape.

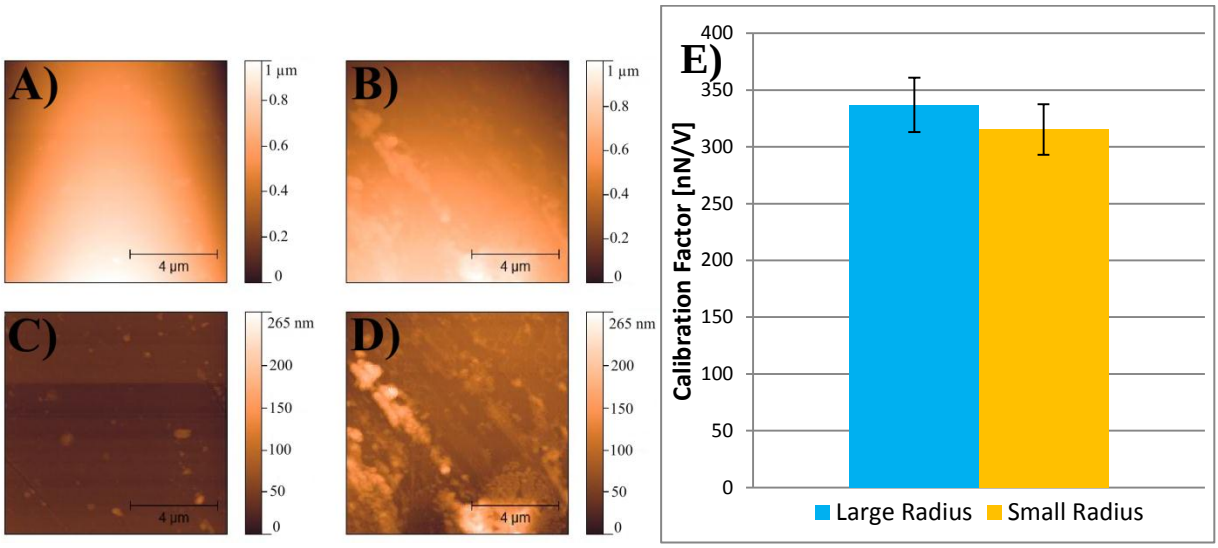

Figure 2.3 – Forward topography at A) small radius (28.9 µm) and B) large radius (98.1 µm) of a pulled micropipette. Leveled images of C) small radius and D) large radius to show the large difference in local topography. The RMS roughness of C) is 4.4 nm and for D), it is 24.2 nm. E) Shape-independence is shown from calibration factors found from A) and B), which differ in radius as well as local topography. The calibration factor is independent of sample shape because the lateral force is calculated from the measured slopes of the sample surface. The averages and standard deviations are calculated from five sets of images.

The relationship between the average lateral force and average lateral voltage must be linear in order that this approach be valid. Linearity depends on the deformation profile of the cantilever, the linearity of the photodetector's response, and the profile of the reflected laser light at the photodetector. To date, all cantilevers tested have behaved linearly; this method is thus far independent of cantilever geometry.

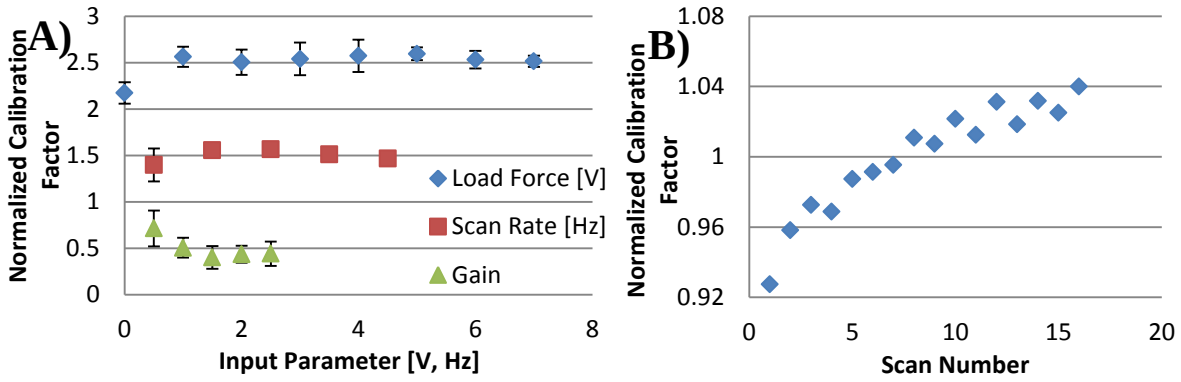

Figure 2.4 – Parameters for which the calibration factor β was A) independent and B) dependent. The calibration factors have been normalized to one and are unitless. The normalized calibration factors for each parameter in A) were offset for clarity. The calibration factor at zero load force was statistically smaller, possibly due to the error in the measured adhesion (see supplemental information). The number of samples used to calculate error are 3, 5, and 5 for the load force, scan rate, and gain respectively. The error bars cannot be seen in some cases because they are obscured by the data points. This shows that the calibration factor was independent of load force, gain, and scan rate. B) The calibration factor increased slightly with each subsequent set of images, probably due to wear of the tip.

Figure 2.4A shows normalized calibration factors as a function of the scan parameters (load force, scan rate, and gain). The calibration factor was found to be independent of each of these parameters as seen from the error bars. The only point of concern is the statistically-significant lower calibration factor for a set point of 0 Volts. Error analysis of the lateral force equations suggests that there is a significantly larger error in the calibration factor at zero load-force (see page 59). Figure 2.4B shows the behavior of the calibration factor as a function of scan number. The slight increase in calibration factor for each subsequent image is probably due to wear of the tip [50]. The standard deviation of the calibration factor among the 16 sets of images is only about 3%. Yet only one set of images—or even a set of partial images—is needed in order to obtain the calibration factor. A description of successful calibration with partial images can be found in the Tip Wear section of Appendix I – Supporting Information for Chapter 2.

2.4 Conclusion

This calibration technique has been shown to produce precise (<10%) calibration factors independent of shape (Figure 2.3), load force, gain, and scan rate (Figure 2.4A) in a quick and simple manner, which will enable better comparisons of nano- and macro-scale friction data. By basing the technique on the measured angles of a sample, instead of on a sequence of loads, the calibration requires only one set of images [45]. The entire calibration process can take as little as fifteen minutes and is primarily limited by the time taken to calibrate the normal spring constant of the cantilever. Future work includes determining the accuracy, investigating partial imaging, comparing with other techniques, and determining friction coefficients for standard combinations of tip and sample materials. An investigation of the effects of cross-talk as others have done is also important [7, 8]. The ultimate goal is to make the calibration traceable to national measurement laboratories, such as the National Institute of Standards and Technology.

3. High-Throughput Method for Force-Curve Analysis

3.1 Introduction

Force curves (FCs) obtained from a scanning probe microscope provide a powerful insight into materials properties. They have been used to determine many different surface parameters in a variety of fields. One such field is the study of bacteria and the formation of biofilms—colonies of bacteria and other microorganisms that are responsible for billions of dollars in damage as well as a vast number of infection-related fatalities [12, 13]. FCs are used to investigate forces at the bacterial surface that are involved with biofilm formation in an ultimate effort to prevent formation altogether.

Bacteria have a layer of polymers on their outer membranes known as lipopolysaccharides (LPS) that are toxic and assist in adhesion [15, 51]. FCs from atomic force microscopes (AFMs) have been used to investigate adhesive and repulsive forces on these LPS brushes to obtain surface parameters for different strains and mutations of bacteria and other surfaces covered with polymers [9, 15, 20, 21, 25, 26]. They have also proven useful to examine how these quantities change in response to external stimuli, such as changes in environmental conditions [18, 23-26]. The surface parameters are typically measured by modeling the forces during the indentation of an AFM tip into a LPS brush, and fitting the model to experimental data. Details such as the average length of LPS and their density can be extrapolated using this method.

There can be a significant amount of variability even between cells of the same strain and population [15, 21, 52]. To combat this, a large population of cells must be probed to accumulate sufficient statistics in order to show trends. This is a problem because models often apply only to a specific region of a FC, and the processing and fitting of several FCs can be time consuming. This has led researchers to either use relatively small sample sets or take shortcuts with their analyses, such as averaging FCs and fitting the average [16, 21, 23, 25, 26]. Either of these time-saving techniques can be detrimental to the validity of the results.

Described here is an objective, accurate, and high-throughput method for analyzing FCs. It was developed to remove subjectivity and increase time efficiency in FC processing, fitting, and analysis. Whereas it can take upwards of twenty hours to manually obtain results from one thousand force curves, this technique can do so in less than one hour. It also eliminates the subjective variability from the choice of the fitting window and the rejection of anomalous FCs and results. Furthermore, it implements several statistical concepts to maximize the precision of the experimental results, which is useful for demonstrating statistical significance.

3.2 Force Modeling and Application

The model most often used [15, 18-24] to calculate the force between an AFM tip and a brush of polymers originates from an equation derived by S. Alexander and P.G. de Gennes which describes the pressure between two polymer-grafted plates in a surface forces apparatus [17].

$$P = \frac{k_B T}{s^3}\left[\left(\frac{2L}{D}\right)^{9/4} - \left(\frac{D}{2L}\right)^{3/4}\right], \tag{3.1}$$

where k_B is Boltzmann's constant, T is the temperature, s is the polymer grafting distance, L is the equilibrium brush layer thickness, and D is the distance between the two plates. This model can be adapted for AFM tips by integrating Equation 3.1 with respect to the cross-sectional area of the tip and replacing $2L$ by L to account for polymer coverage on only one surface.

Detailed derivations can be found in Appendix III – Alexander-de Gennes Force Model Derivations — the following are the results for spherical, conical (circular cross-section), and pyramidal (square cross-section) geometries, respectively:

$$F_{spherical} = \frac{8\pi k_B T R L}{35 s^3}\left[7\left(\frac{L}{D}\right)^{5/4} + 5\left(\frac{D}{L}\right)^{7/4} - 12\right], \tag{3.2}$$

$$F_{conical} = \frac{32\pi k_B T L^2}{385 s^3}\tan^2\theta\left[77\left(\frac{L}{D}\right)^{1/4} + 33\frac{D}{L} - 5\left(\frac{D}{L}\right)^{11/4} - 105\right], \tag{3.3}$$

and,

$$F_{pyramidal} = \frac{128 k_B T L^2}{385 s^3}\tan^2\theta\left[77\left(\frac{L}{D}\right)^{1/4} + 33\frac{D}{L} - 5\left(\frac{D}{L}\right)^{11/4} - 105\right]. \tag{3.4}$$

In the preceding equations, R is the tip radius and θ is the half angle of the cone or pyramid. To our knowledge, this is the first appearance of the conical and pyramidal models in the literature. The differences in the behavior of each model can be observed in Figure 3.1.

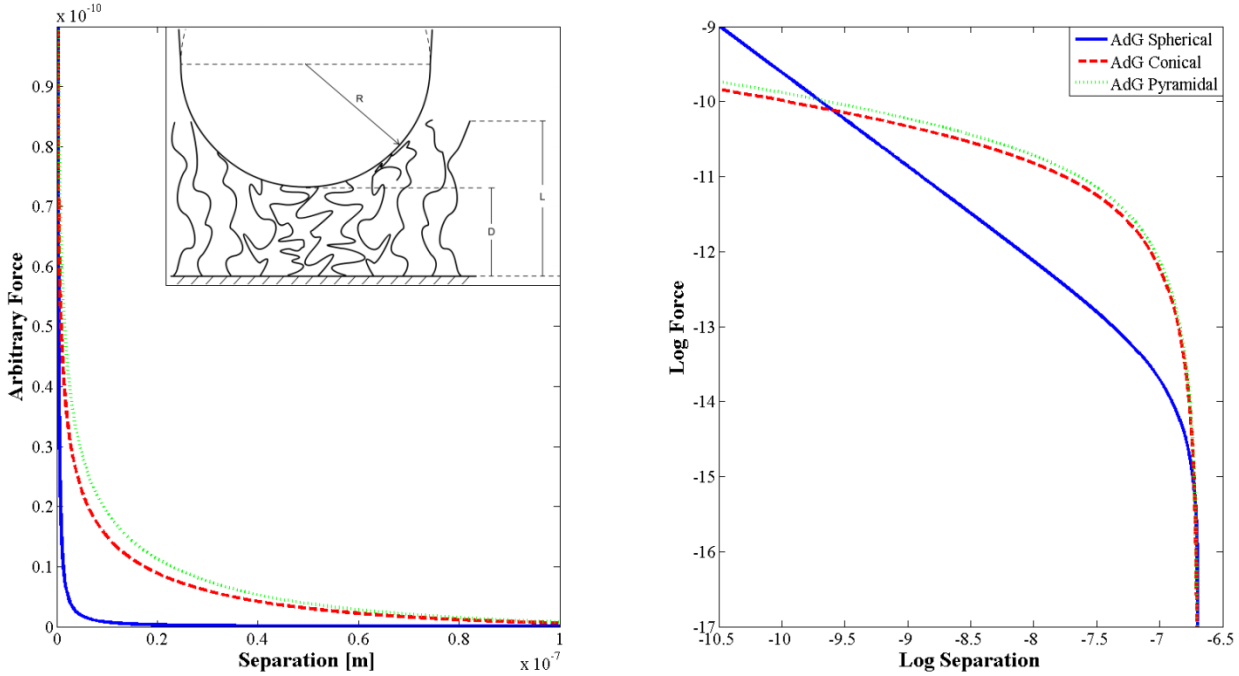

Figure 3.1 – A comparison of the force models for the different tip geometries. A trivial coefficient has been used to set each model to the same scale, so the force axis is arbitrary. The slope of the logarithmic curves (right) are the exponents of the dominant terms from their respective force models. This slope is used to determine where the experimental data deviate from the model. The slope is *-5/4* for the spherical model and *-1/4* for the pyramidal and conical models.

These equations can be used to fit experimental AFM data from polymer brushes, including bacteria, but are only applicable to a certain region of the FC. All models are applicable only after contact has been made, or when $D \leq L$. The spherical model is only valid while the tip can be approximated as a sphere (see inset of Figure 3.1), or where $L - R \leq D \leq L$. This implies that contact marks the larger separation bound of the fitting window, or the region of the FC where the model may be applied. The smaller separation bound is determined from the behavior of the model at low separations where the L/D term dominates; when the experimental data deviate from this term, the model is no longer applicable. This is most easily visualized in a log-log force vs. separation plot, because the

terms involving D are then linear. The exponents of the D/L terms will be manifested at large separations (where they dominate) and the L/D terms can be seen at small separations with either a $-5/4$ or $-1/4$ slope, depending on the model. Deviation from these terms can be thought of as a coupling of the bacterial membrane with its surface polymers which may occur at large forces. The tip radius has been used as the smaller separation bound of the fitting window in the past, but this is the first time the log-log slope has also been used. In the case of the spherical model, the smaller separation bound is determined by whichever constraint comes first.

3.3 Materials and Methods

3.3.1 Original Experimental Design

The original objective of this study was to observe how the bacterial LPS brush reacted to changes in pH. It has been shown that the LPS length increases with pH for the bacterium *Acidithiobacillus ferrooxidans* [26], but there have been little to no such studies with *Pseudomonas aeruginosa*. It is hypothesized that the LPS repel each other more with increasing pH leading to an increased brush thickness. The conformational change in the LPS should therefore be evident in FCs taken with an AFM.

3.3.2 Atomic Force Microscopy

An Asylum MFP3D AFM was used to image and obtain FCs on *Pseudomonas aeruginosa* bacteria in the presence of phosphate buffered saline (PBS) to simulate *in vivo* conditions. The procedure for preparing the bacteria can be found in Appendix IV – Sample

Preparation. After an image was acquired, ten bacteria were chosen and ten FCs were taken in the center of each of the selected bacteria. The previous buffer was then removed, PBS with a different pH was introduced, and the procedure was repeated. PBS with pH 4, 5, 6, 7, and 9 were used, and the experiment was performed in a pyramid-type fashion, varying from pH 4 to 9 and then 9 to 4. One thousand FCs in total were obtained from each experiment (ten per bacterium, ten bacteria per pH, and ten pH scenarios).

The cantilever spring constant was calibrated using the Asylum MFP3D software and a method similar to Matei et al. [49]. First, the resonance frequency and the normal deflection sensitivity are measured. The deflection sensitivity was always determined using a glass slide to ensure the constant compliance region of the FC was reached. The movement of the cantilever due to thermal energy is observed, and the Fourier transform is fit with the equipartition theorem. The theorem relates the average thermal energy of the cantilever to its average spring potential energy, which contains the spring constant. Veeco DNP D cantilevers were used for all experiments (triangular, 0.06 N/m).

The tip radius was determined by scanning across a TGT01 delta-function grating purchased from Mikromasch. A sphere was fit (by eye) to a cross section of the tip image to measure the tip radius. This method will not be accurate if the tip is sharper than the features of the grating, which is possible if the grating endures significant use. This was tolerated because of the focus on FC treatment and analysis rather than quantitative considerations.

3.3.3 Matlab Programming

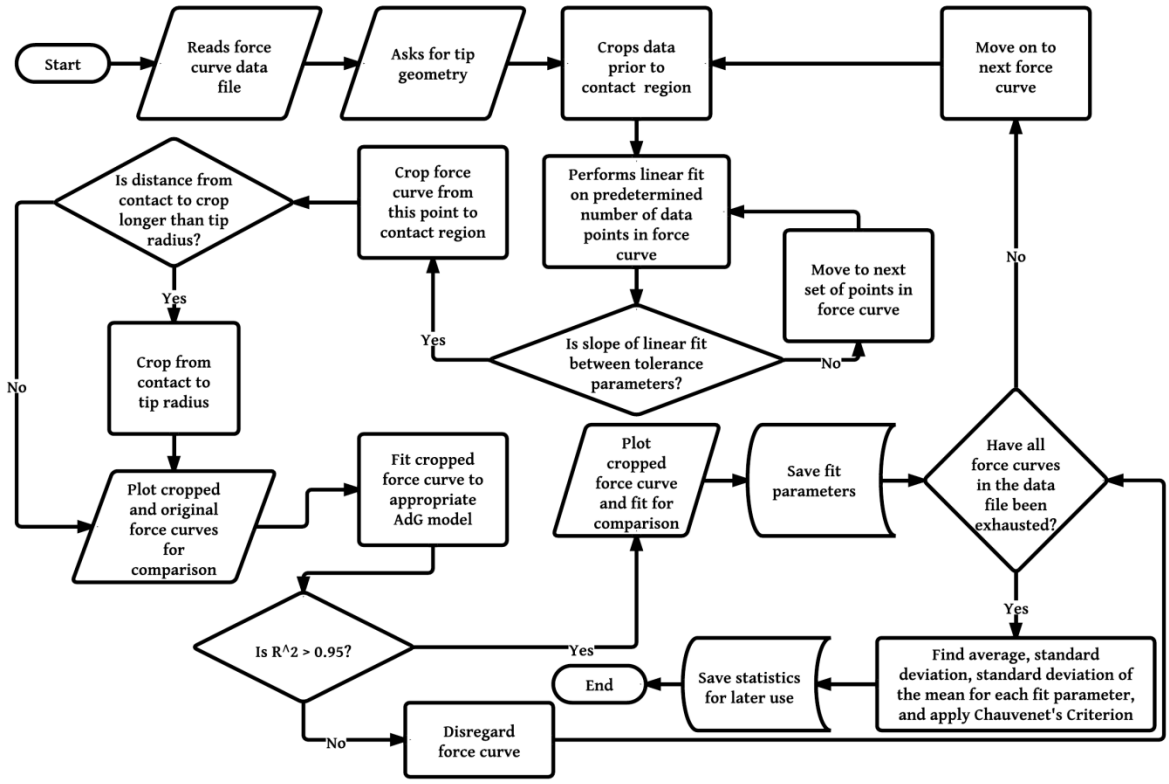

Figure 3.2 – A flowchart summarizing the processes automated by Matlab. The program objectively crops and fits a group of force curves, and then it applies Chauvenet's Criterion to remove outliers in an effort to increase the precision of the fitted parameters. The automation greatly reduces the time needed to crop and fit a large number of force curves. Whereas experiments with hundreds to thousands of force curves could take tens of hours to analyze, the program can do the same objectively in less than one hour.

Matlab 2011a was used to write and run the program detailed in this paper. The flowchart in Figure 3.2 describes the steps taken by this program to crop, fit, and analyze each FC. It begins by reading the file containing the FC data, and asks if the tip geometry is spherical, conical, or pyramidal (each of the geometries is described by a different force model and has a different fitting window). One FC is analyzed at a time until the force data have been exhausted.

The point of contact is determined by the Asylum MFP3D software, and all data prior to contact are cropped. The smaller separation bound of the fitting window is then found by fitting the FC with a series of linear fits in a log-log plot. When the slope of the FC in the log-log plot deviates from *-5/4* (spherical), or *-1/4* (conical and pyramidal), the model is no longer applicable for reasons explained in Section 3.2. The FC is cropped from the smaller separation bound of the window to the end of the FC. If a spherical tip geometry was used, the model is longer applicable if the tip indents the LPS past its radius. The program decides if the cropped FC describes brush indentation that is larger than the tip radius, and if so, it crops the FC from contact to the tip radius. The FC before and after cropping are plotted next to a *-5/4* slope line to demonstrate the effectiveness of the crop (as seen in Figure 3.3, right).

The FC is fit using the appropriate force model (Equation 3.2 for spherical, 3.3 for conical, or 3.4 for pyramidal) and the nonlinear fitting function from the Matlab Curve-Fitting Toolbox. The fit is rejected unless its R-squared value is higher than 0.95 (which can be adjusted by the user). If the fit meets this criterion, the results are saved and the next FC is fit. The original data and the fit are plotted together to visualize how well the data agree with theory (as seen in Figure 3.4).

Two concepts from statistics were employed in an effort to reduce error bars so that trends could be more easily discerned: standard deviation of the mean and Chauvenet's Criterion. The former has been used before in the literature concerning bacteria because of the potentially large cell-to-cell variance [15]. The standard deviation of the mean is defined

by $\sigma_{\bar{x}} = {}^{\sigma_x}/_{\sqrt{N}}$, where σ_x is the standard deviation and N is the number of samples used in its determination. This reduced error bars by up to an order of magnitude in this investigation because one hundred force curves were obtained for each experimental condition.

Chauvenet's Criterion is a method used to objectively remove outliers, but has not been commonly applied to bacteriology. The mean and standard deviation of a data set are calculated, and the probability of each datum point occurring based on the probability density function (Equation 3.5) is multiplied by the number of data points in the set. If the result is less than one half, the datum may be discarded. A new mean and standard deviation can be calculated after the outliers have been removed, and the criterion may be applied again.

$$f(x) = \frac{1}{\sigma\sqrt{2\pi}} \exp\left[\frac{-(x-\bar{x})^2}{2\sigma^2}\right]. \tag{3.5}$$

Chauvenet's Criterion can be written mathematically as $P(x)N < 1/2$, where $P(x)$ is the probability of obtaining the datum, x, and N is the number of data points ($P(x) = \int_x^{\infty} f(x)dx$ if $x > \bar{x}$ or $P(x) = \int_{-\infty}^{x} f(x)dx$ if $x < \bar{x}$). The criterion is performed by the program until no further data can be discarded from a particular set.

3.4 Results and Discussion

The program successfully crops, fits, and analyzes large sets of FCs (tested up to 120 curves) much faster than can be done manually. Before the program, the author could crop and fit a single FC in slightly less than one minute where the program does so in fractions

of a second. The implementation of the program greatly increased data processing efficiency and allowed for the acquisition of larger data sets and therefore better statistics. This is significant because sound statistics are needed to compensate for the large amount of cell-to-cell variance in bacteria. The surface parameters between bacteria of the same population can vary significantly [15, 21, 25, 52].

3.4.1 Program Effectiveness

FC cropping proved more difficult than originally thought due to the amount of noise in the FCs. The correct number of points must be chosen for the linear fit (used to find the slope) based on the number of datum points in the FC; if too few points are used, the fit becomes sensitive to noise, and if too many points are used, the linear fit will be applied to nonlinear data. There was significantly less noise while the cantilever was in contact so it was much easier to determine where the larger separation bound of the fit window should be. It was often found that the larger separation bound due to the tip radius (~40 nm) was more constrictive than the *-5/4* region. The same method was attempted to find the point of contact, but did not work as well due to the amount of noise in the free-equilibrium region of the FC. It is for this reason that the AFM software was allowed to determine where contact begins.

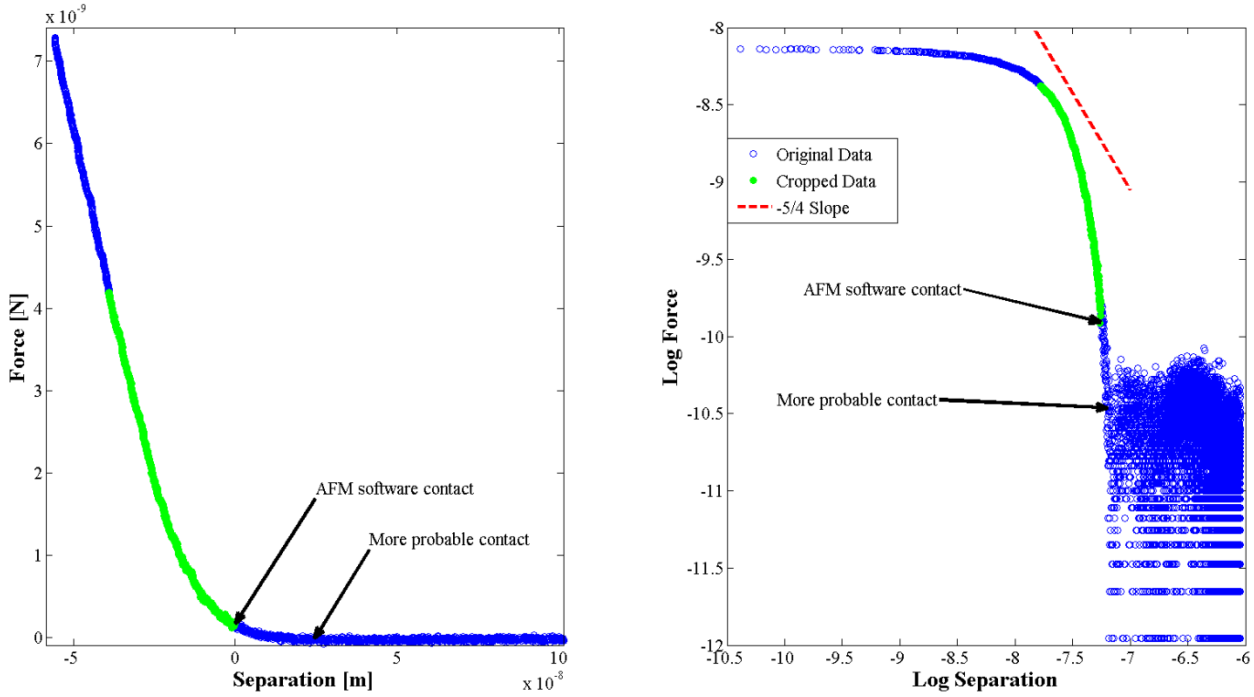

Figure 3.3 – Linear (left) and logarithmic (right) plots showing the original (blue/dark) and cropped (green/light) force curve from the Matlab program. The Alexander-de Gennes force model is only applicable from where contact begins to the point where the membrane of the bacterium begins to significantly deform. The deformation of the membrane is manifested by a deviation from the -5/4 slope (dashed line). This comes from the force model in which the 5/4 term dominates for low separations; when the curve deviates, the model is no longer applicable. The Matlab program determines where this deviation occurs through linear fits to the logarithmic data. Membrane deformation is determined when the slope of the linear fit is within a user-defined tolerance of -5/4. The contact region is currently determined by the AFM software (MFP-3D Igor Pro), but will be implemented into the Matlab program in the near future. The data points organized horizontally in the bottom of the image on the right correspond to the sensitivity of the photodiode (~0.2 mV).

Figure 3.3 shows how effectively the program is able to crop a single FC. The slope of the FC may not match up exactly with the *-5/4* slope because a tolerance is set within the program to allow for some slight deviations. It is also clear from this figure that the AFM software did not choose the contact region correctly but was off by a couple of nanometers. The software's definition of contact is best suited for stiff surfaces, so it was not expected to be perfect in its application to bacteria. Independent determination of contact will be

implemented in a future version of the program, perhaps by measuring the noise level of the approach region and defining contact as where the FC rises three standard deviations above it (99.7% of the data of a normal distribution lie within three standard deviations from the mean). It is important to determine contact accurately because the most significant curvature occurs just after contact, as can be seen from Figure 3.3. The amount of curvature directly influences the L and s parameters, and less curvature can result in unrealistically large values for both.

Up to 120 FCs were fit at once, taking about 30 seconds to complete. Fits with R-squared values less than 0.95 were rejected providing the first criterion for rejection of 'bad' data. Figure 3.4 shows how the shape of the FCs affects the fitting results. The data on the left show typical results, with L of 150 ± 30 nm. The data on the right exhibit unbelievably large values for L, 1094 ± 763 nm, even after the application of Chauvenet's Criterion. This is believed to be attributed to a miscalculation of the contact region, as depicted in Figure 3.3.

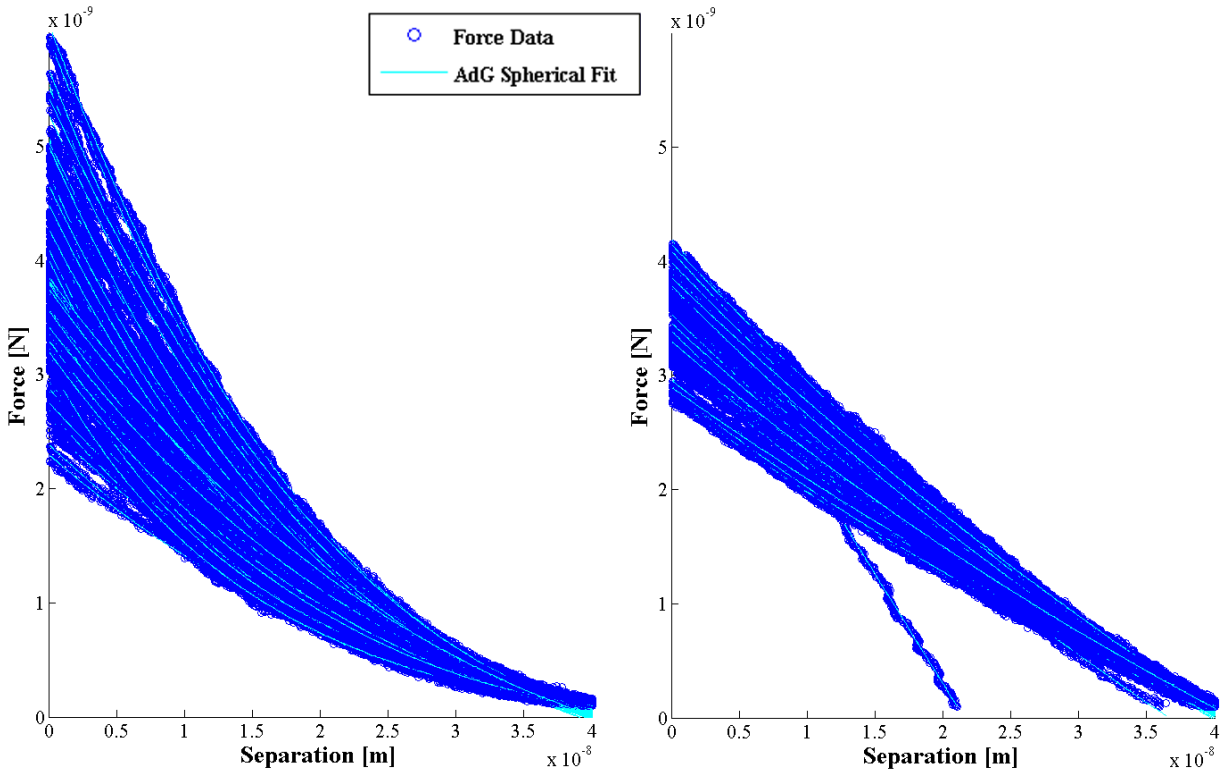

Figure 3.4 – AdG spherical fits for a set of force curves with normal fitting results (left) and extraordinarily large *L*'s (right). The plot on the left contains 120 force curves, none of which were removed by Chauvenet's Criterion. *L* for these data was found to be 150 ± 30 nm. The plot on the right contains 98 force curves, before six of which were removed by Chauvenet's Criterion. *L* was found to be 1094 ± 763 nm. The plot on the right exemplifies how the miscalculation of the contact region leads to larger fit parameter values, because the lower the curvature in the data, the larger the *L*. Note that the x-axis has been shifted so each force curve lines up in a way which they can be compared.

The constriction of using only fits with R-squared values greater than 0.95 helped to eliminate some suspicious results—usually fits that produced unrealistically large values for *L*. The LPS length for *Pseudomonas aeruginosa* (ΔWzz1 mutant) is expected to be in the hundreds of nanometers range [15], but fits sometimes yielded *L's* on the order of micrometers. These suspect data points skew the average and standard deviation of the

results dramatically, but without scientific outlier-removal criteria, their omission would be subjective.

3.4.2 Increasing Precision

The use of the standard deviation of the mean, constraint of acceptable R-squared values, and Chauvenet's Criterion helped to drastically reduce error bars and show statistical significance. Overall, the standard deviation decreased by about 145% using these three concepts in conjunction.

The standard deviation of the mean increased the precision by about an order of magnitude on average because of the number of FCs obtained (100-120) for each condition. This affects only the error bars and some of the average results from fitting were still skewed by suspected outliers. It did, however, provide the greatest increase in precision for statistical significance comparisons.

Creating a standard for acceptable fits provided an objective manner for removing suspicious FCs. Only a small portion of FCs was rejected from this R-squared standard (~2-3%). The removed FCs were most likely ones that could not be zeroed properly (due to a sloped approach region) or that slipped off the bacterium during probing.

Chauvenet's Criterion was the most necessary statistical concept used in this investigation to achieve believable results. On average, the criterion reduced fitting parameters by over 20% and standard deviations by 64%. It can be seen from Figure 3.5 how most of the fitting results lie on left side of the probability distribution while some

suspect data lie far to the right side, skewing the average and standard deviation. The data in Figure 3.5 constitute an extreme case where 26 out of 98 points were omitted by Chauvenet's Criterion; it typically removed less than 10% of the data. The objective elimination of outliers successfully decreased the average values of L to within a believable range of 100-500 nm.

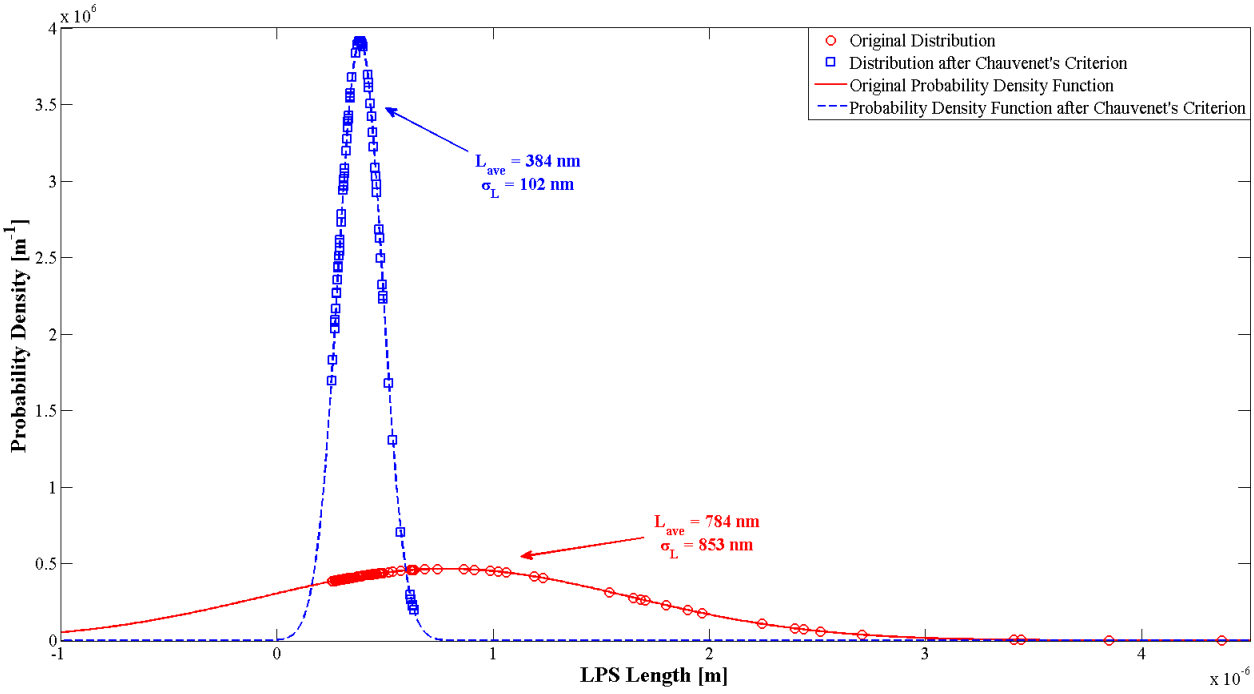

Figure 3.5 – This figure demonstrates the effect of Chauvenet's Criterion on a set of fit values with a particularly large standard deviation. The red circles show the distribution of the fit parameter that describes the lipopolysaccharide (LPS) length of the bacterium *Pseudomonas aeruginosa*, and the red line is a normal probability density fit to those data. The blue squares represent the LPS length distribution after the application of Chauvenet's Criterion, an objective method to remove outliers, and the dashed blue line is a fit to those data. Chauvenet's Criterion removed 26 of the 98 data points from the original set, reducing the average and standard deviation by 51% and 88% respectively. It should be noted that the 72 data points that remain are difficult to discern in the original distribution because they are so closely clustered.

The original Gaussian in Figure 3.5 is particularly suspicious due to the significant negative portion, which implies there is a probability that L is less than zero. This is a

consequence of the large standard deviation in the data. The large standard deviation comes from the few fits that produce exceptionally large values for L. We believe this is a result of an improper determination of the contact region in the FC. It has been seen that larger values for L are obtained from FCs with less curvature, as would be seen if contact was determined to occur later than in reality. However, Chauvenet's Criterion was able to discard FCs where contact had presumably been miscalculated, as is clear from Figure 3.5.

3.5 Conclusions

Overall, the program is able to effectively crop and fit 120 FCs in about one minute. This is a significant improvement from manual cropping and fitting with roughly 120:1 increase in time efficiency. The program also removes subjectivity from the cropping, fitting, and outlier-removal process which has been seen to induce large changes in fitting results. It has also implemented statistical concepts that increase fitting measurement precision to improve the resolution to observe trends in experimental data. With this progress, we hope to inspire greater care with FC fitting, analysis, and statistics.

4. Appendices

4.1 Appendix I – Supporting Information for Chapter 2

4.1.1 Calibration Program

The calibration program exploits the linearity between lateral force and voltage to obtain the calibration factor. Figure 4.1 is a flow chart that shows the basic operations executed by the calibration program.

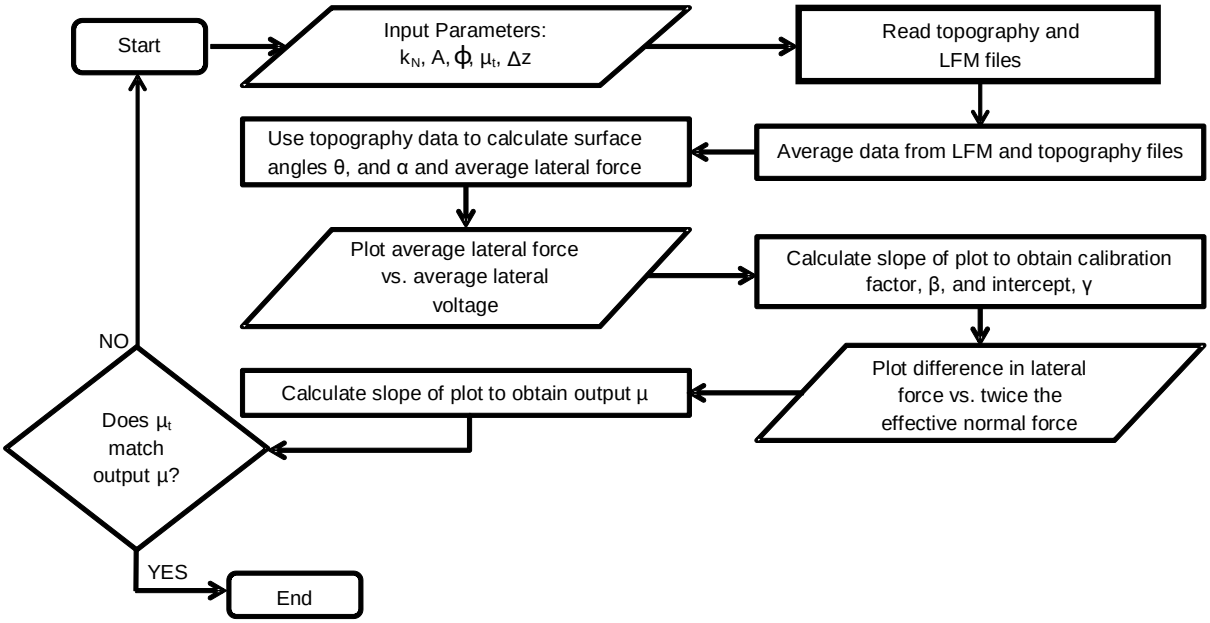

Figure 4.1 – These are the general steps taken by the calibration program in order to obtain a calibration factor and intercept. The needed input parameters are the normal spring constant, k_N, the average sample adhesion, A, the cantilever angle of repose, φ, a trial value for the coefficient of friction between the tip and sample, μ_t, and the change in scanner height required to impose the desired load force on the cantilever Δz.

The parameters needed to find the calibration factor are: the normal spring constant, k_N, the angle of repose of the cantilever, φ, the average adhesion between the tip and sample, A, the trial coefficient of friction, μ_t, and the scanner displacement used to image at constant force, Δz. The product of the normal spring constant and the scanner displacement ($k_N \Delta z$) is equal to the product of the load force and the cosine of the angle of repose ($F_{load} \cos\varphi$). The program first averages the forward and reverse topography and LFM files. It then calculates the slope at each point using the averaged topography data.

The average lateral force in nanoNewtons, $\bar{F}_{lat}$, (Equation A1.1) is then plotted against the average lateral force in Volts, $\bar{V}_{LFM}$. The difference in lateral force (Equation A1.2) is then plotted against twice the effective normal force (everything but μ in Equation A1.2).

$$\bar{F}_{lat} = F_{load} \cos\varphi \tan\theta \left[\frac{1+\mu_t{}^2 \cos^2\alpha(1+\tan\alpha \tan\varphi \sec\theta)}{1-(\mu_t \cos\alpha \tan\theta)^2}\right] + 2A \left[\frac{\mu_t{}^2 \cos\alpha \tan\theta \sec\theta}{1-(\mu_t \cos\alpha \tan\theta)^2}\right]. \quad \text{(A1.1)}$$

$$\Delta F_{lat} = \frac{2\mu}{\cos\theta} \left[\frac{F_{load} \cos\varphi \cos\alpha(\sec\theta+\tan\varphi \tan\alpha)+2A}{1-(\mu_t \cos\alpha \tan\theta)^2}\right]. \quad \text{(A1.2)}$$

The user then modifies the value for the trial coefficient of friction (in Equation A1.1) and runs the program again until the output value of the coefficient of friction (in Equation A1.2) converges to the trial value. The least-squares fit of the average lateral force plot then gives the calibration factor as the slope ß of the fitted line, as well as the intercept ɣ.

$$\bar{F}_{lat} = \beta \bar{V}_{LFM} + \gamma. \quad \text{(A1.3)}$$

The slope and intercept can then be used to convert LFM voltage into lateral force as shown in Equation A1.3.

The program is freely available at www.wpi.edu/+afm.

4.1.2 Calibration Accuracy

The accuracy of the calibration procedure was tested on an order-of-magnitude level by comparing experimental torsional spring constants with those obtained from geometry. The tip height and cantilever thickness were measured in a scanning electron microscope to minimize uncertainty. The experimental and geometric torsional spring constants are given in Equations A1.4 and A1.5, respectively.

$$k_{exp} = \omega\beta\chi\,, \tag{A1.4}$$

$$k_{geo} = \frac{Gwt^3}{3lh^2}\,, \tag{A1.5}$$

where in Equation A1.4 ω is the torsional sensitivity of the system in [V/nm$_{scanner}$], β is the calibration factor in [nN/V], and χ is the ratio of the movement of the scanner to the lateral movement due to the twisting of the cantilever in [nm$_{scanner}$/nm$_{tip}$]. In Equation A1.5, G is the shear modulus, w is the cantilever width, t is the thickness, l is the cantilever length, and h is the tip height.

The experimental torsional spring constant is constructed by measuring the torsional sensitivity ω, the calibration factor β, and calculating the ratio of movements χ. The torsional sensitivity is measured by finding the average of the slopes of the forward and reverse startup artifacts in a typical lateral force voltage profile. The AFM was set to

scan so that there was minimal scanning movement and the majority of the profile was due to static friction. A measuring process in SPMLab software that averages thirteen adjacent lines in the LFM profile was used. Three of these averages were used for each of the forward and reverse startup artifacts, and then the average of the forward and reverse slopes was taken to obtain the final torsional sensitivity.

The ratio of displacement from cantilever twisting to lateral motion of the scanner was found from Equation A1.6.

$$\Delta x_{total} = \Delta x_{twist} + \Delta x_{lat} + \Delta x_{sample}, \quad \text{(A1.6)}$$

where Δx_{twist} is the displacement due to the twisting of the cantilever, Δx_{lat} is the displacement of the tip from the lateral bending of the cantilever, and Δx_{sample} is the displacement due to the deformation at the tip-sample interface. It was assumed that the displacement of the tip at the tip-sample interface was small (i.e. that the deformation at the tip-sample interface was negligible). Equation A1.7 is the result of solving for the ratio of the lateral displacements of the scanner and tip.

$$\chi = \frac{\Delta x_{total}}{\Delta x_{twist}} = 1 + \frac{4Gt^2l^2}{3Ew^2h^2}, \quad \text{(A1.7)}$$

where E is Young's modulus of the cantilever.

The results for calibration accuracy are summarized in Supplementary Figure 1 where the x-axis is the spring constant obtained from Equation A1.5 and the y-axis is the constant from Equation A1.4. It was pleasantly surprising to find that these values were within 65% of each other from this order-of-magnitude investigation. The overall accuracy

was 38±19% with errors as small as 17%. Accuracy will be a central theme in the future development of this technique.

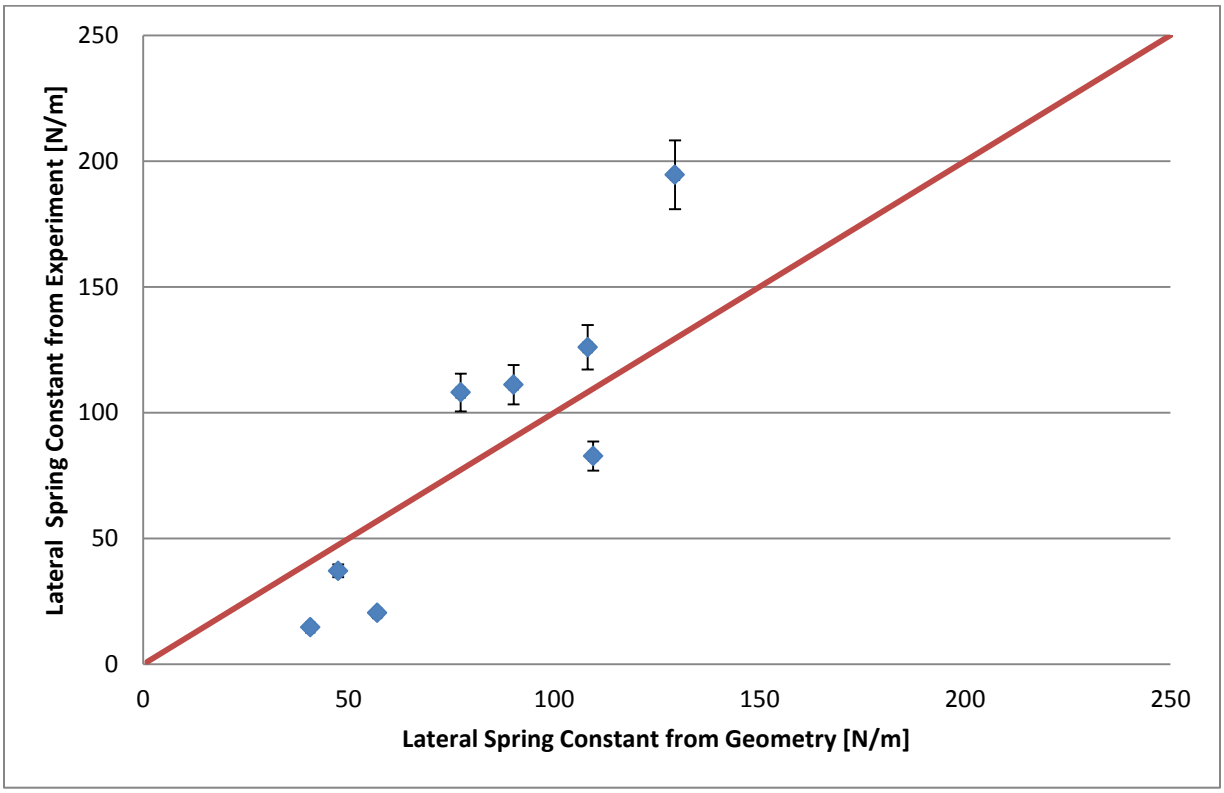

Figure 4.2 – Calibration accuracy comparing the lateral spring constant found from experiment (Equation A1.4) with that found from geometry (Equation A1.5). The straight line indicates perfect agreement. Error bars are 7% of calibration factor which was the typical precision of any experiment. The goal was to determine if the lateral spring constants were within a factor of ten of those found from geometry; they were within 65%.

4.1.3 Error Analysis

The average lateral force (Equation A1.1) was analyzed to determine the principal source of error in the limits of zero adhesion and zero load force. Equations A1.8 and A1.9 are obtained from error analysis, whereby small terms in denominators (μ^2) and terms with *tan a* in them have been dropped for clarity.

$$\frac{\delta \bar{F}_{lat(A=0)}}{\bar{F}_{lat}} = \sqrt{\begin{array}{c}\left(\frac{\delta F_{load}}{F_{load}}\right)^2 + \left(\frac{\delta \cos\varphi}{\cos\varphi}\right)^2 + \left(\frac{\delta \tan\theta}{\tan\theta}\right)^2 + \left(\mu^2 \cos^2\alpha\right)^2 \left[\left(\frac{\delta\mu}{\mu}\right)^2 + \left(\frac{\delta \cos\alpha}{\cos\alpha}\right)^2\right] \\ + \left(2\mu^2 \cos^2\alpha \tan^2\theta\right)^2 \left[\left(\frac{\delta\mu}{\mu}\right)^2 + \left(\frac{\delta \cos\alpha}{\cos\alpha}\right)^2 + \left(\frac{\delta \tan\theta}{\tan\theta}\right)^2\right]\end{array}}$$

(A1.8)

$$\frac{\delta \bar{F}_{lat(F_{load}=0)}}{\bar{F}_{lat}} = \sqrt{\begin{array}{c}\left(2\frac{\delta\mu}{\mu}\right)^2 + \left(\frac{\delta A}{A}\right)^2 + \left(\frac{\delta \cos\alpha}{\cos\alpha}\right)^2 + \left(\frac{\delta \tan\theta}{\tan\theta}\right)^2 + \left(\frac{\delta \sec\theta}{\sec\theta}\right)^2 \\ + \left(2\mu^2 \cos^2\alpha \tan^2\theta\right)^2 \left[\left(\frac{\delta\mu}{\mu}\right)^2 + \left(\frac{\delta \cos\alpha}{\cos\alpha}\right)^2 + \left(\frac{\delta \tan\theta}{\tan\theta}\right)^2\right]\end{array}}$$

(A1.9)

The error in each term is represented with the symbol *δ(term)/(term)*, which is the standard deviation divided by the average. The principal source of error in the zero-adhesion case (Equation A1.8) is the load force (10%). In the zero-load-force case (Equation A1.9), the same error comes from the adhesion measurement (10%), but there is also a large error in the coefficient of friction (10%, but effectively 20% due to the factor of two). These results suggest that that there is a large error in the calibration when performed at zero load-force, and this should be avoided if possible. This probably explains why the calibration factor at zero load-force was significantly different in Figure 2.4 of Chapter 2.

A compromise must be made between minimizing error and tip wear. While imaging at high-load forces minimizes error, it increases tip wear; imaging at low-load forces minimizes tip wear, but increases error.

4.1.4 Tip Wear

Although some techniques require no contact for LFM calibration, these types of calibrations either calibrate a test cantilever or are *ex-situ* [36, 40, 43, 44]. The advantage of the shape-independent calibration procedure is that the probe is calibrated in the same manner as it will be used, despite the presence of some tip wear. One way to minimize tip wear in calibration procedures that require contact is to use small imaging areas; by scanning a smaller area, the tip is subject to less wear. The precision of the calibration factor was investigated using partial images to simulate smaller scan sizes. Figure 4.3 summarizes the results of this analysis. Three sets of images were taken on the same spot of the micropipette using the same scan parameters. The calibration program was used to crop rows of data and the calibration factor was found as a function of the number of rows of data. The number of rows can then be converted to scanning area using pixel resolution and the size of the image. Rows were cropped, twelve at a time, until only four were being used in a 256 x 256 pixel image. This was done for all three sets of images to obtain average and standard deviations of the calibration factor as a function of scanning area. The standard deviations are biggest when a small scanning area is used, as expected. These data show that a valid calibration factor can be obtained using only part of an image, which can help limit tip wear.

Tip wear can also be reduced by using lower-load forces. It can be seen from the Error Analysis section that the calibration error becomes more dependent on the adhesion as the load force decreases. Future work will concentrate on reducing the error that

accompanies calibration with low-load forces, where adhesion plays a dominant role. For example, adhesion could be measured at more points to use local adhesion values in the calibration program. Once the low-load limit is more accurate, it may be more reliably used to help reduce tip wear.

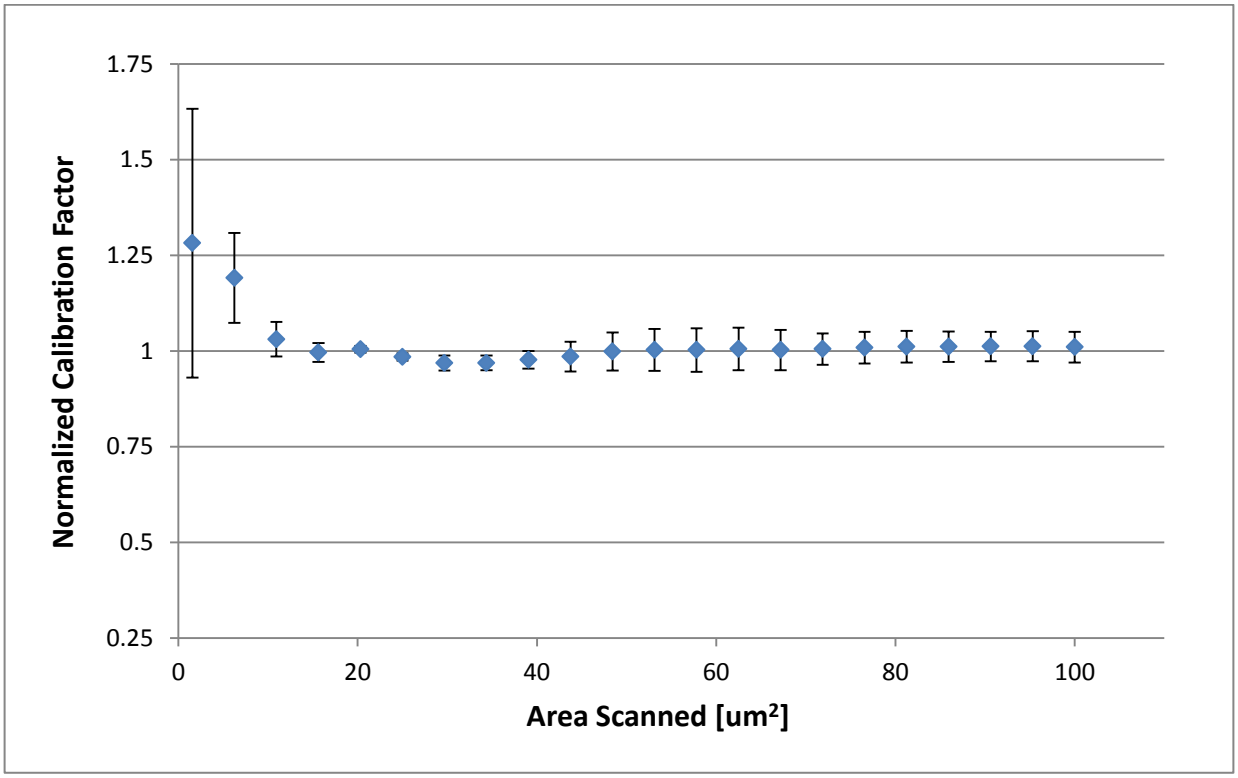

Figure 4.3 – A normalized average calibration factor was obtained as a function of the scanning area from three sets of images. The images were taken using the same scan parameters on the same spot of the micropipette. Twelve rows at a time were cropped out of the sets of images and a calibration factor was obtained, until there were only four rows out of a 256 x 256 pixel image. The number of rows can be converted to scanned area using the pixel resolution and the size of the image. This was done for each of the three sets of images and the calibration factors were averaged for each scanned area. The standard deviation shown is calculated using the three calibration factors produced from each set of images. This result shows that a valid calibration factor can be obtained using partial images, thereby limiting tip wear.

4.1.5 Interpretation of the Coefficient of Friction

More research is needed to interpret the coefficient of friction obtained from the calibration program. The plot for the difference in lateral force against twice the effective normal force yielded linear results when using the test files for the cone and sphere, as was expected. The slope of this plot is the coefficient of friction, μ (Equation A1.2). The plots of the experimental data were never linear to the extent of the test file data, but typically produced reasonable and repeatable results. The shape of the experimental plots looked more like a vertically-oriented oval, where the majority of the data approximated a line. Typical values for the coefficient of friction were between 0.1 and 0.5.

Unusual coefficients were occasionally obtained, as low as 0.05 and as high as 0.8. They were either larger than expected (sometimes greater than one) or negative. The shapes of the coefficient of friction plots were visually different, sometimes appearing like a histogram on its side. These unexpected coefficients were not repeatable and require further investigation. This behavior could reflect a non-uniform coefficient of friction across the sample.

The coefficient of friction only appears as a second-order term in the model, and plays a secondary role in determining the calibration factor. Yet future work will focus on understanding experimental coefficient-of-friction data. The model can also be revised to accommodate different friction laws (as opposed to Amontons' law).

4.1.6 Detailed Experimental Section

4.1.6.1 Pulled Micropipette

A pulled micropipette was used as the sample for all of the experiments performed in this study. A normal micropipette is heated in the center and pulled apart using a micropipette puller. The result is a sample that is macroscopic (several centimeters) along its length, but can reach microscopic diameters (under 100 nanometers) at the end where it was separated. (The diameter can be established from a cross-section of an image and simple geometry.) This makes for a convenient and inexpensive sample because it provides a large range of angles at its microscopic end, but is still easy to work with because of its macroscopic length.

4.1.6.2 Normal Spring Constant Calibration

The normal spring constant was calibrated using a thermal method as described Matei et al [49]. The procedure measures the resonance frequency and the normal sensitivity of the cantilever. The thermal spectrum of the cantilever is then fit in order to find the normal spring constant. This is done using the equipartition theorem, which relates the average thermal energy to an average spring potential. The normal spring constant was measured this way before and after each experiment, and the average was used for all calculations. The range of spring constants for the cantilevers used in these experiments was from 0.070 to 9.0 N/m. All cantilevers were silicon, with manufacturer's tip radii stated as 10-20 nm.

4.1.6.3 Adhesion Measurements

Adhesion was measured by taking force curves over the length of the image. The AFM (a Bruker Autoprobe M5) was set up to take the average of 16 force curves at 16 different points along the long axis of the pipette. The maximum pull-off force was measured after being converted to adhesion force using the normal spring constant of the cantilever. The adhesion was then calculated by averaging the adhesion of the 16 points.

4.1.6.4 Load Force

A Mikromasch CSC12 C lever was used for this experiment. The load force was varied in a pyramid-type fashion, varying the set-point from 0 V to -7 V in 1 V increments (0 to -7 and then -7 to 0). A total of three sets of images were acquired for each set point. The scan rate was 1 Hz for all images, and the gain varied from 0.9 to 1.2 depending on the set point.

4.1.6.5 Scan Rate:

A Mikromasch CSC12 F lever was used for this experiment. The scan rate was varied in the same pyramid-type fashion as mentioned for load force, varying from 0.5 to 4.5 Hz by intervals of 1 Hz. A total of four sets of images were taken for each scan rate. A set point of -5 V was used for all images, and the gain varied from 2 to 2.5 depending on the scan rate.

4.1.6.6 Gain

A Mikromasch NSC12 F lever was used for this experiment. Images were taken at -5 V set point. The gain was varied in the pyramid-fashion mentioned above, from 0.5 to 2.5 in

increments of 0.5. This was repeated until four sets of images at each gain were acquired. All images were acquired at a set point of -5 V and 1 Hz.

4.1.6.7 Sample Wear

A Mikromasch NSC12 E lever was used for this experiment. The AFM scanned 25 x 25 μm at -4 V set point and 1 Hz for about 70 minutes, resulting in 16 consecutive sets of forward and reverse topography and LFM images.

4.1.6.8 Error and Precision Calculations

All errors mentioned were calculated by dividing the standard deviation of a data set by its average and multiplying by 100%. Typically, the precision of the calibration factor was 7%.

4.2 Appendix II – LFM Calibration Procedure

This section outlines a step-by-step process to calibrate a cantilever for lateral force microscopy. The exact steps and terminology are based on the Veeco Autoprobe M5 microscope, but will be the same in principle for any microscope.

4.2.1 Step 1 – Thermal Calibration (for determination of the normal spring constant)

1) After mounting the cantilever to be calibrated and aligning the laser, find the resonant frequency of the cantilever (Laser off, Setup->Configure Parts: choose NCM for Head Mode and AFMNCM for M5 Mechanical Switch then turn the laser back on and click Yes). Record the frequency of the lowest-frequency peak. (NOTE: it is good practice to leave the light for the optics off after finding the cantilever, as the light will add thermal energy to the system and it will take longer to reach equilibrium.)
2) Turn the laser off, and return to Setup->Configure Parts to change the Head Mode back to AFM.
3) Approach a stiff surface to calibrate the optical lever sensitivity; mica, glass, or the AFM stage will do.
4) Once in contact, turn off Z Servo (the feedback loop, in image mode) and ScanMaster.
5) In Input Configuration (Setup Menu), choose Z Detector and CN7 Aux (essentially the raw A-B signal).
6) Choose X-Y Trace (Tools Menu).
7) Change the range to -0.5 to 1 and click Sweep.

8) After one sweep, click Stop and set the Horizontal Axis to Z Detector.
9) Click on the CN7 window (the bottom plot) and check View One (at the top).
10) Click Sweep again until a decent force curve is acquired, usually after one or two sweeps, then click Stop.
11) Select Measure at the top.
12) Left-click on one of the traces at the top left of the force curve (upper end of constant compliance region) before it becomes flat (photodiode is saturated) and then right-click at the bottom right of the curve where it is still linear (lower end of constant compliance region). DO NOT MOVE THE CURSOR.
13) Record the values for dx and dy. These will be your values for Δz and ΔV respectively.
14) Turn ScanMaster and Z-Servo back on and raise the scan head fully.
15) Turn Z-Servo and Scan off (Z-Servo unchecked, Scan Off is a button) and allow the cantilever time to reach thermal equilibrium with its surroundings (usually about 15 minutes).
16) Turn on the oscilloscope and log into the data acquisition computer. Ensure that the raw A-B BNC port of the signal access module is connected to Channel 1 of the oscilloscope.
17) Open up all of the programs under the Thermal K folder: set_oscope.vee, read_ave.vee, Data Acquisition, and fit.mcd.
18) After the cantilever has had time to equilibrate, run the set_oscope program to prepare the oscilloscope for data acquisition.

19) On the Data Acquisition program, choose Instrument, select 54620, hit OK, and select All Points. Agree that you are willing to wait a couple of minutes to record over two million data points. This is the thermal noise in the A-B signal.
20) After a waveform appears on the screen, you may select File->Save As and save the waveform under C:/User Programs/Thermal/Intuilink as the next waveform (i.e. waveform34) with the extension .csv.
21) Bring up the read_ave program and calculate $\Delta z/\Delta V$ that you recorded earlier keeping the negative sign.
22) Enter this value into the box at the top of the screen above the plot and click Run.
23) Select the waveform you just saved and hit OK.
24) After a short time, the program will ask you to save a file named bee.txt. Agree to save this file, and overwrite the previous version.
25) Bring fit.mcd to the front and enter the resonant frequency you measured in the yellow box marked by v_0.
    a. OPTIONAL: To compare your measured spring constant with the theoretical spring constant from geometry, enter the values for the dimensions of the cantilever in their respective boxes.
26) Click on the bee.txt icon and hit F9 to refresh the file.
27) Scroll down to the bottom of the page and a light bulb will indicate that the program is trying to fit the FFT (Fast Fourier Transform) of the thermal noise. Refer to the paper by Matei and Burnham from 2006 to understand the physics behind this fit [49].

28) Check the plot of the Gaussian curve to make sure you have a good fit. The blue line represents the fit while the red dots are the data. If your fit isn't good, try measuring the resonant frequency again or waiting longer for equilibrium.

29) If the fit is good, record all of the data in green boxes at the bottom. A1 is the 1/f noise, B1 is the white noise, Q is the quality factor, v_k is the resonant frequency, $\langle x^2 \rangle$ is the mean-square amplitude, k_t is the thermal spring constant (the one you are probably after), and k_{geo} is the spring constant calculated from geometry.

4.2.2 Step 2 – LFM Calibration Data Acquisition

1) First, calibrate the optical lever sensitivity (for the AFM program) on a stiff surface such as mica, glass, or the AFM stage. If you will always be doing thermal calibration beforehand, it would be convenient to add this step between step 12 and 13 of thermal calibration. (NOTE: the sensitivity depends on the spot of the laser on the cantilever; do not move the laser after recording the sensitivity).
    a. Approach the surface and come into contact.
    b. Choose Scan Off in Image Mode.
    c. Open Spectroscopy Mode.
    d. Click Run and wait for a decent force curve. All you really need is a good range of the constant-compliance region (the sloped, linear region).
    e. Click Cal Sweep, and then Setup.
    f. Enter the spring constant you measured from thermal calibration, and make sure Z-Detector is selected as well as Snap-Out. Click OK.

g. Click Run again and then Stop after one decent force curve is acquired.
h. Select Measure and left-click the upper left part of the force curve before the signal becomes saturated (flat-lines).
i. Right-click the bottom right part of the force curve where it is still linear. Try to make sure both clicks were on the same trace (extension or retraction).
j. Click Calibrate.
k. Click Run again to make sure the y-axis is in some order of Newtons as opposed to Volts.

2) Mount the pulled micropipette on the stage as perpendicular as possible to the edge of the stage near the opening in the acoustic hood. Also make sure that the side with the putty is facing the opening in the hood so that the scanner does not touch it.
3) The goal now is to 'land' the cantilever on top of the pipette. This can be tricky so here are a couple tips.
    a. First, get comfortably close to the pipette by eye.
    b. Close the hood and focus the optics as far down as possible. If the optics are off, you should turn them on now.
    c. Slowly lower the scan head until either the sample holder or the pipette come into focus.
        i. If you can't see the pipette at this point, you will have to slowly move the stage around until you do see it. It can be helpful to check inside the hood periodically to try and judge how to move the stage.

d. Once you've found the pipette, center it on the screen as best you can and focus back up on the cantilever.

4) Now you should compare the size of the scan you want to perform with the diameter of the pipette in the area of the cantilever. The goal is to get as much variance in the lateral force as possible without saturating the signal. The pipette diameter should be similar to the scan size.
5) Approach the pipette with the mouse over the Stop button in case the cantilever looks like it is going to miss the pipette.
6) Once in contact and scanning, choose forward and reverse Topography and LFM from Input Configuration (-> is forward and <- is reverse).
7) If you will be performing a second thermal calibration after lateral calibration, now is a good time to turn the optics off again.
8) Monitor the LFM trace to ensure you have a chosen a good spot on the pipette for your desired scan size. The LFM voltage ranges from -10 V to 10 V; you want to come as close to these extremes as possible without saturation (which will appear as a suspiciously-flat line on the trace).
    a. Either choose a different spot or scan size to correct for this.
9) Take an image. The LFM signal is a better gauge of the optimal gain; it should not be oscillating (as would be seen with a gain set too high) because this will affect the calibration.

a. Because the pipette is also sloped in the y-direciton, it is possible the piezo will reach the limit of its extension or retraction towards the end of the image. Try approaching again and taking another image if this is the case.

10) After the image is done, click Scan Off and open Spectroscopy Mode.
11) Click Run and adjust the extension and retraction to get a decent force curve.
12) Draw a line from the top of the topography image to the bottom, ideally along the apex of the pipette. This is the line along which the AFM will take 16 force curves.
13) Click Acquire. If you see that most of your force curves saturate upon retraction due to large adhesion, you may need to offset the laser on the photodiode to a positive voltage and try acquiring again.
14) You should now have 16 buffers (0-15) of force curves (each averaged from 16 force curves). Select Measure and left click on the baseline of the first force curve.
15) Move the cursor down to the bottom of the adhesion "trough" and read dy without moving the cursor. This is the adhesion force for that spot on the pipette.
16) Record the adhesion force for each buffer and find the average.
17) You may now raise the scan head and remove the sample.

4.2.3 Step 3 – Calibration Program

1) Export your four images from the AFM using a CD.
2) Use SPMLab to open your images.
3) Export each image as a text file using File->Export.
4) Open the calibration program.

5) Enter your scan parameters.
    a. The number of header rows is 18 if you used the Autoprobe and SPMLab.
    b. The number of rows and columns is 256 by default, but will change if you modified the number of pixels to capture on the AFM.
    c. It is wise to crop around 32 columns to remove start-up artifacts.
    d. You may crop rows if you find noise in your images. The cropping function trims both of the edges of the image rather than just from one side.
    e. The angle of repose is 11 degrees for the Autoprobe.
    f. The spring constant is the thermal spring constant you measured, or the average if you measured before and after imaging the pipette.
    g. Δz is calculated by multiplying $\Delta z/\Delta V$ by the set point voltage you used to image the pipette. This is the deflection of the cantilever kept constant by the feedback loop.
    h. The adhesion is the average you calculated from the 16 averaged force curves (256 force curves)!
    i. Do not worry about trial mu for now.
6) Click Start.
7) Choose the files as the window asks for them. The first image should be reverse LFM, the second should be forward LFM, and so on.
8) It will then ask you for filenames to save the resultant plots under. Name them whatever you like.

9) The program will now plot the theoretical lateral force (based on the angles of the sample) against the average lateral voltage as well as the difference in lateral force against twice the effective normal force. Refer to the Shape-Independent Lateral Force Calibration manuscript for the physics [11]. Once the program has fit both plots, compare the mu under the second plot to the trial mu. The goal is to get these numbers to converge. Change the trial mu to a number close to the output mu and click Start.
10) Keep the previous filenames.
11) After the program is done, compare the trial and resultant friction coefficients (mus). Continue until mu is roughly equal within two significant figures.
12) Once the mus are sufficiently close, you may record the calibration factor (ß) and intercept (γ). These can be used to convert lateral voltage into lateral force!

$$\bar{F}_{lat} = \beta \bar{V}_{LFM} + \gamma \quad \text{(A2.1)}$$

13) You can now image your sample of interest. The calibration factor and intercept can be used to convert the scale bar from Volts to nanoNewtons after you have your images.
    a. Remember:
        i. The calibration factor and sensitivity are unique to the spot of the laser on the cantilever; if it is moved, you must re-calibrate.
        ii. Lateral force is not friction! The lateral force is largely dependent on the normal force. You will have to do extra analysis in order to

quantify the friction force (i.e. subtracting out the roles of normal force and adhesion).

4.3 Appendix III – Alexander-de Gennes Force Model Derivations

This appendix gives a detailed derivation for the AdG spherical force model, as well as the beginning and ends of the conical and pyramidal models. The only difference between the derivations for each model is finding the cross-sectional area for each tip as a function of the amount the tip has indented into the polymers.

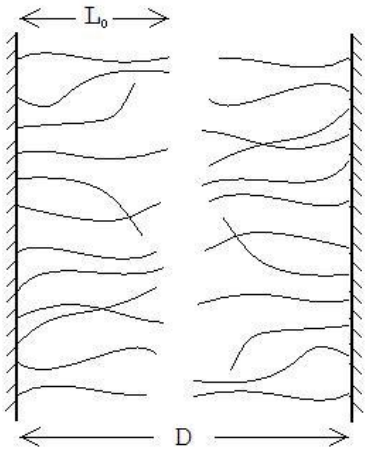

Figure 4.4 – The theoretical scenario investigated by Alexander and de Gennes. The pressure between the two plates is described by Equation 1. This model is the basis for the force models derived in this appendix.

$$P(D) = \frac{k_b T}{s^3}\left[\left(\frac{2L}{D}\right)^{9/4} - \left(\frac{D}{2L}\right)^{3/4}\right]. \quad \text{(A3.1)}$$

All derivations begin with the model developed by Alexander and de Gennes for the pressure between two plates grafted with polymers (see Figure 4.4 and Equation A3.1). In this equation, k_B is Boltzmann's constant, T is the temperature, s is the grafting distance, L

is the equilibrium brush layer thickness, and D is the distance between the two plates. Pressure is related to force by Equation A3.2 and subsequently Equation A3.3,

$$P = F/A, \tag{A3.2}$$

$$F = \int P dA. \tag{A3.3}$$

It can now be seen from Equation A3.3 that the derivations differ only by dA.

4.3.1 Spherical

The spherical model is probably the most difficult as far as finding how the cross-sectional area relates to z, the distance between where the polymers are acting on the tip and the substrate. Please see Figure 4.5 for a depiction of the different variables.

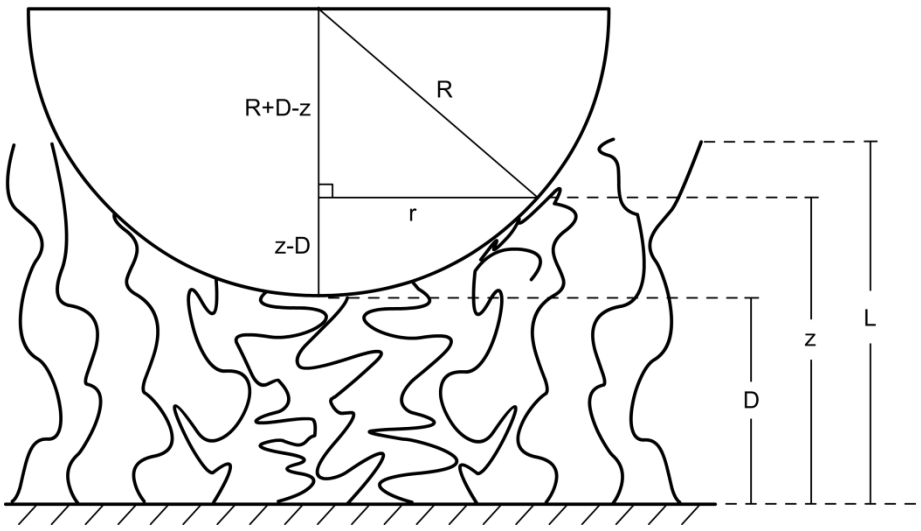

Figure 4.5 – A depiction of the different variables used for the derivation. *R* is the tip radius, *D* is the distance between the tip and the substrate, *z* is the distance between where the polymers are touching the tip and the substrate, *r* is the cross-sectional radius at *z*, and *L* is the equilibrium brush length of the polymers.

The cross-sectional area of a sphere is

$$A = \pi r^2 , \tag{A3.4}$$

and the derivative of that area is

$$dA = 2\pi r dr . \tag{A3.5}$$

We must now relate r and z by

$$R^2 = r^2 + (R + D - z)^2 , \tag{A3.6}$$

which becomes

$$r^2 \approx 2R(z - D) \tag{A3.7}$$

under the assumptions $R>>z-D$ (depending on the experiment, not necessarily true). z is the variable of integration.

$$rdr = Rdz . \tag{A3.8}$$

Combining Equations A3.3, A3.5, and A3.8 gives

$$F = 2\pi R \int P(z) dz . \tag{A3.9}$$

Combining Equation A3.9 and A3.1 gives

$$F = \frac{2\pi R k_B T}{s^3} \int_D^L \left[\left(\frac{L}{z} \right)^{9/4} - \left(\frac{z}{L} \right)^{3/4} \right] dz \quad . \tag{A3.10}$$

Note that *2L* was replaced by *L* in Equation A3.10 because only one surface is grafted with polymers in this case. After integrating, we arrive at the final result,

$$F(D) = \frac{8\pi k_B T R L}{35 s^3} \left[7 \left(\frac{L}{D} \right)^{5/4} + 5 \left(\frac{D}{L} \right)^{7/4} - 12 \right]. \tag{A3.11}$$

It is also important to note that the equation above is only applicable under the following conditions:

$$L - R \le D \le L \tag{A3.12}$$

and

$$\frac{d(\log F)}{dD} \le -5/4 \, . \tag{A3.13}$$

The constraint in Equation A3.12 is due to the fact that the model is only valid while the tip is in contact with the brush, and the tip can still be approximated as a sphere. The other constraint arises because the first term of Equation A3.13 dominates at small values of *D*; when the slope begins to deviate, the model is no longer applicable. This can be attributed to deformation of the bacterial membrane (or whatever the substrate happens to be).

Note that the same basic approach applies to parabolas [18] of the form $z - D = r^2/2R$, with the advantage that integration need not stop if $z - D > R$. Because, the tip

radius was easier to fit to a sphere than a parabola, we applied the spherical model. Note also that the assumption of $R \gg z - D$ used to reach Equation A3.7 does not hold for tips that are small compared to the layer thickness, as was true for this study. However, the emphasis in this study was on data handling, and better matches between tip shape and models are reserved for future work.

4.3.2 Conical

The derivation of the conical model is very similar to that of the spherical model. In fact, it is much easier to relate *r* and *z*. All of the variables used are defined in the same manner as in Figure 4.5. The only new variable is the half angle of the cone, θ. The cross-sectional areas and derivatives thereof are the same for a sphere and cone (see Equations A3.4 and A3.5). The variables *z* and *r* are related by,

$$\tan\theta = \frac{r}{z - D}. \tag{A3.14}$$

The cross-sectional area is then,

$$A = \pi(z - D)^2 \tan^2\theta. \tag{A3.15}$$

The derivative is then

$$dA = 2\pi(z - D)\tan\theta dz. \tag{A3.16}$$

z is the only integration variable. Equation A3.16 can be inserted into Equation A3.3 to arrive at

$$F(D) = \frac{32\pi k_B T L^2}{385 s^3} \tan^2\theta \left[77 \left(\frac{L}{D}\right)^{1/4} + 33\frac{D}{L} - 5\left(\frac{D}{L}\right)^{11/4} - 105 \right]. \quad \text{(A3.17)}$$

The equation above is only applicable under the following conditions:

$$0 < D \leq L \quad \text{(A3.18)}$$

and

$$\frac{d(\log F)}{dD} \leq -1/4. \quad \text{(A3.19)}$$

These constraints arise from the same reasoning as in the spherical model.

4.3.3 Pyramidal

The pyramidal model is somewhat different from the other two because the cross-sectional area of a pyramid is a square. Otherwise, it is almost identical to the conical model. The cross-sectional area is

$$A = (2r)^2 = 4r^2, \quad \text{(A3.20)}$$

where *2r* is the length of one side of the square made by the cross-sectional area. The variables *r* and *z* have exactly the same relation as in the conical derivation, following Equation A3.20. The cross-sectional area is then

$$A = 4(z - D)^2 \tan^2\theta, \quad \text{(A3.21)}$$

and its derivative is

$$dA = 8(z - D)\tan\theta dz\,, \tag{A3.22}$$

The equation above only differs from Equation A3.16 in the pre-factor, which is why the result is so similar,

$$F(D) = \frac{128 k_B T L^2}{385 s^3}\tan^2\theta\left[77\left(\frac{L}{D}\right)^{1/4} + 33\frac{D}{L} - 5\left(\frac{D}{L}\right)^{11/4} - 105\right]. \tag{A3.23}$$

The constraints for this equation are the same as for the conical model, and can be found in Equations A3.18 and A3.19.

4.4 Appendix IV – Sample Preparation

4.4.1 Cleaning Glass Slides

1) Cut slides (optional).
2) Wash slides with Mili-Q water.
3) Sonicate slides for 15-30 minutes.
4) Soak slides in 3:1 Hydrochloric acid (HCl) / Nitric acid (HNO_3) for at least 25 minutes.
5) Wash slides with Mili-Q water.
6) Soak slides in 7:3 Sulfuric acid (H_2SO_4) / Hydrogen peroxide (H_2O_2) for about 1 hour.
7) Wash slides with Mili-Q water.
8) Store in Mili-Q water, in refrigerator.

4.4.2 LB Broth

1) Combine LB Broth with Mili-Q water using 25 g/L.
2) Heat and stir at about 300°C until LB is completely dissolved.
3) Autoclave using liquid cycle #2 (about 1 hour).

4.4.3 LB Agar Plates

1) Combine LB Agar with clean water using 0.7 g per 20 mL (20 mL for each plate) in a flask.

2) Stir with magnetic stir bar on a hotplate at about 300° C until the mixture begins to smoke.
3) Autoclave using liquid cycle #2 (about 1 hour).
4) Pour LB Agar into Petri dishes (~20 mL for each plate) and let sit for about 1 hour.
5) Seal with Parafilm for later use or plate bacteria for growth.

4.4.4 Growing Bacteria

1) Pour 50 mL of LB Broth into a glass flask under a sterile vacuum hood.
2) Proceed to a) if growing from stock, and b) if growing from plates.
    a. Take the appropriate vial of bacteria from the -80° C freezer and add it to the LB broth.
    b. Scrape the plate with an inoculation loop until a pellet of bacteria fills the loop. Then shake the pellet off into the LB broth.
3) Place the flask in an incubator for desired growth time (author typically used 10-13 hours).

4.4.5 Plating Bacteria

1) Grow bacteria and have agar plates ready.
2) Stir inoculation loop in bacterial solution in order to form a meniscus in the loop (under sterile hood).
3) Wipe loop across the surface of the agar plate as much as desired.
4) Use Parafilm to seal plate.

5) Place plates with bacteria-side facing down in 37° C room.
6) Place plates in refrigerator once bacteria have grown sufficiently (about 10-15 hours for the author).

4.4.6 Phosphate-buffered Saline (PBS)

1) Combine packet of PBS with prescribed amount of water. PBS concentration is 0.1 M and the pH should be around 7.4.
2) Autoclave liquid cycle #2 (optional, if sterile PBS is desired).

4.4.7 EDC

1) Combine 0.096 g of EDC with 5 mL Mili-Q water.
2) Lower pH of EDC solution to between 5 and 6 using diluted sulfuric acid (H_2SO_4).
3) Store in refrigerator (lasts about one week).

4.4.8 NHS

1) Combine 0.0435 g of NHS with 5 mL clean water.
2) Raise pH of NHS solution at least 10 using sodium hydroxide (NaOH), and then lower pH to between 7 and 8 using additional NHS (once the pH gets near 7, it will quickly approach 12 or so making it difficult to not surpass the 7-8 range, but this is okay and possibly even necessary).
3) Store in refrigerator (lasts about one month).

4.4.9 Bacteria Binding Procedure

1) After growing, pour 10 mL of bacteria into each of two centrifuge tubes and centrifuge on level 7 for 10 minutes.
2) Rinse clean slides in methanol.
3) After first centrifuge cycle is done, pour out liquid from centrifuge tubes without losing bacteria and add 10 mL of water.
4) Disperse the bacteria in water using a transfer pipette and centrifuge again.
5) Add 1:1 ratio of 3-Aminopropyltrimethoxysilane:methanol to centrifuge tube and mix using the mini vortexer.
6) Pour aminosilane solution onto glass slides and leave covered for at least 20 minutes.
7) Repeat steps 2-4.
8) After third centrifuge cycle is complete, pour out the water as described before, but add only 5 mL of water to each tube.
9) Disperse the bacteria in each tube and combine into one.
10) Add 300 µL EDC and then 600 µL NHS to bacteria solution and tilt tube back and forth during remaining steps if possible.
11) Rinse the slides with water and add to new Petri dish after at least 20 minutes has passed since adding aminosilane.
12) Pour bacteria solution onto slides and shake on the shaker table for at least 2 hours before imaging.

4.5 Appendix V – Force Curve Processing and Analysis

4.5.1 Program Summary and Author's Notes

The purpose of this appendix is to walk through the data processing and analysis of force curves (FC's) from the export stage to results. These programs were written in an attempt to create a high-throughput method for processing and analyzing FC's so that a sufficient sample size may be used in order to achieve satisfactory statistical analysis in a reasonable time. Follow this appendix, and you should be able to analyze an entire experiment in a fraction of the time it would take to do manually.

These instructions are intended for the Asylum MFP3D AFM with Igor Pro software, but can theoretically be applied to any AFM as long as the exported FC's come out the same. Please see the flowchart from Chapter 3 (Figure 3.2) for a quick understanding of what these programs do.

4.5.2 Exporting Force Curves from Igor

1) Plot waves (FC's) to export in Igor (MFP3D) using the Review button on the Force Panel.
2) Plot deflection as a function of separation and ensure all FC's have the correct InvOLS in the Parm tab.
3) Zero the FC by first clicking on the Y-Offset button then on the Raw Offset button.
4) Click Edit on the force plot.

5) From the dropdown menu at the top of the screen, click Data->Save Waves->Delimited Text.
6) Select all of the FC's in the left column, check Modified Only and Interactive and then click Do It.

Unfortunately, the exported file organizes all of the separations and deflections separately so another program is needed to sort this out (suitably known as FC_sort.m).

4.5.3 Sorting Force Curves (FC_Sort.m)

This program is only necessary if the exported force curves you receive from Igor are not in the correct order (i.e. separations are together, separate from forces). It was written to treat the way force curves came out for me, and may not be appropriate for other exporting mishaps. After importing the tab-delimited text file into Excel, the first half of the columns contained force data while the second half contained separations. I found an algorithm to sort this out (empirically). A more difficult, but robust method would be to have Matlab search for the wave number corresponding to the separation and force for a particular force curve and stitch them together that way.

1) Run the program and select the Excel file containing the jumbled data.
2) Save the resulting file.

You can test this program to see if it will work for your data by labeling the first few separation columns something like 1.1, 1.2, 1.3, etc. and then the first couple force columns 2.1, 2.2, 2.3, etc. If you click and drag from the bottom right of the last cell when all three

are highlighted, Excel will understand your naming convention for the subsequent cells. This way, you can name all of the forces 2.X while their corresponding separations are named 1.X. After running the sorting program, the data should be in the order: 1.X, 2.X, 1.X+1, 2.X+1, etc. and you can be sure the file was properly sorted!

4.5.4 Cropping Force Curves (FC_Crop.m)

The cropping program is probably the most important in this series of Matlab scripts. It will automatically crop FC's down to the applicable region of the Alexander-deGennes force model as long as the previous two steps were done correctly. You will need to know both the spring constant of the cantilever and the radius (or angle) of the tip in order to get accurate results.

1) Run the program and choose the properly-sorted data file.
2) You are given the option to crop all of the data contained in the file, or to manually choose a portion (a handy UI feature actually lets you select the data to crop out of Excel if this option is chosen).
3) The program will then ask what type of tip you were using—spherical, conical, or pyramidal. Most tips can be approximated as spheres at their very end, so this may be the safest bet if you are unsure (but you should find out). The purpose of this is to set the log-log slope the data should have for very small separations (*-5/4* for spherical, *-1/4* for conical and pyramidal).

a) If a spherical tip is chosen, the program will ask if you would like to consider the tip radius for cropping (recommended). This will yield more accurate results.

4) The last question the program asks is if you would like to plot the resultant cropped FC's in order to compare them with the original. This is certainly recommended especially if you haven't cropped this particular file before.

5) Behind the scenes (in the code):

   a) There are various constants that are contained in the code of the program at this step that set how far to translate the force curves before plotting, and the thresholds for finding the upper bound of the FC to crop.

   b) Determines the number of FC's in the file (number of columns divided by two) and their lengths (number of rows).

   c) Creates a progress bar to display how far through the file the program is.

   d) Takes the first FC:

      i. Separates FC into force and separation.

      ii. Crops the region before contact as set by Igor by removing points with separation greater than zero.

      iii. Translates the FC into the first quadrant in order to take the natural log of the force and separation data.

      iv. Does linear fits to a number of points (42 by default), starting from the left-hand side of the curve, and checks the slope to see if it is within a

threshold set within the program (parameters a, upper-bound tolerance for slope, and b, lower-bound tolerance for slope).

1. If the slope isn't within the threshold, the program moves on to the next 42 points.
2. If it is within the threshold, the program notes the index of the point where the linear fit was done, and crops data before that point (from left to right).
3. If the length of the FC is exhausted before finding this region, it will result in a warning message after the program has cropped all of the FC's in the data file. The message will state how many FC's failed to fall within the threshold set by the user and suggest tweaking.

e) For spherical tips only:

i. If the user chose to use the tip radius to crop the FC, the program will compare the length of the FC cropped from contact to the -5/4 region to the tip radius.

1. If the tip radius is bigger, the -5/4 region determines the upper bound and no further cropping is done.
2. If the tip radius is smaller, the FC is cropped from the point of contact to that value less the tip radius.

f) The program will then create four plots, two linear and two logarithmic, for the FC before cropping and after cropping. The program then moves on to the next FC.

g) After all FC's have been plotted, the program will plot several red lines with slopes equal to either -5/4 or -1/4 depending on the tip geometry in the cropped logarithmic plot. Several had to be used to ensure they would overlap different sets of data, but will contort the scale. Use the zoom function to magnify the left-hand region of the cropped logarithmic curves to ensure the slope is similar to that of the red lines.

6) The program then asks if you would like to save the cropped curves.

7) Possibly helpful naming convention example: pH4CS40 would pertain to a file for pH 4 that has been cropped with spherical geometry in mind and used a tip radius of 40 nm. CC and CP could be used for cones and pyramids, respectively.

The cropped data is now ready to be fit with FC_Fit!

4.5.5 Fitting Force Curves (FC_Fit.m)

The fitting program is the last in the necessary Matlab programs. In order to obtain accurate results, you should know: the spring constant (probably already implemented), the tip radius (for the spherical model) or the tip half-angle (for conical and pyramidal models), and the temperature. The angles of the tips for conical and pyramidal models are especially important to know well because a 5° error can result in pre-factors that differ by an order of magnitude.

1) Run the program and select the cropped data file.
2) As with the cropping program, a portion of the file may be chosen for fitting as opposed to the entire file.
3) The program asks which model you would like to fit to your data. The different models are suitable for different tip geometries.
4) The program needs to know the tip radius (for the spherical model) or the half angle of the tip for conical and pyramidal models.
5) Only FC's with R-squared values greater than 0.95 (changeable) are plotted or recorded.
6) You may choose to plot the fits in order to see how well they agree with the experimental data.
7) Behind the scenes:
    a) There is a vector containing starting values for the model, a requirement of the nonlinear fit function. These values may be changed within the program.
    b) A progress bar similar to the one in the cropping program is created so the user has an idea of how far through their data set the program is.
    c) Zeroes are converted into NaN's (not a number) so the program does not try to fit irrelevant data. Globs of zeros are created at the end of FC's so that all FC's in the matrix are the same length—an annoying result of automation which has thankfully been worked around.

d) The FC is then fit by the chosen model. Some FC's may end up with complex parameter results, so a warning was created to notify the user after the program is done of how many FC's returned complex parameters. The nonlinear function cannot be forced to only real parameters.

e) The fitting parameters are saved if the R-squared value is greater than whatever it has been set to. The FC is then plotted along with the fit on both linear and logarithmic scales.

f) After all of the FC's have been exhausted, the program finds the number of FC's with good fits, the average values for each parameter, the standard deviation, and the standard deviation of the mean for each parameter.

8) The program then asks if you would like to remove outliers from the results using Chauvenet's Criterion (see Section 3.3.3 for background).

    a) If 'Yes' is chosen, Chauvenet's Criterion is applied to the set of results repeatedly until no further outliers can be removed.

9) The option is then given to save the parameter results into an Excel file for later comparison.

The next two programs may be helpful for data comparison, but are optional.

4.5.6 Comparing Results from One Experiment (Results_Compare.m)

This program is useful for visualizing the results of a single experiment. It will be helpful to run your results through this program first if you would like to compare results from different experiments. You will need to have saved the results from FC_Fit.m in order for this program to work properly. Alternatively, you can manually create Excel files if you see how the saved results are ordered.

1) Select the number of results files you have to compare from the menu after running the program. This is the number of files you ran through FC_Fit.m for which you would like to compare fitting results.
2) The program will ask you to select these files, and will remember the order in which you selected them. Make sure you also remember this order, as you will need to use it later.
3) The program asks if you would like to use standard deviation or standard deviation of the mean for your error bars.
4) A dialog box will come up asking for what you are varying (i.e. Temperature or pH). This just gives the x-axis a label.
5) Another dialog box pops up asking for the values used for the experimental variable in the order that the files were imported. Enter these separated by spaces (i.e. 4 5 6 7 or 4 4 5 5 6 6 etc.).
6) The program will then plot L and s by default, while h can also be included if you uncomment it inside the code.

7) The program then asks if you would like to save these results. If you would like to compare between experiments it is recommended you do. The results are saved in a .mat file for use in the next program.

4.5.7 Comparing Results from Several Experiments (Experiment_Compare.m)

This program is used to compare results between experiments. You will need to have saved your results from Results_Compare.m in order to effectively use this.

1) Run the program and a dialog box will pop up asking how many experiments you would like to compare. It will ask you to select as many .mat files as you requested to compare. These are the files that were saved from the Results_Compare.m program.
2) It then asks if you would like to use standard deviation or standard deviation of the mean.
3) The program then uses (a much more efficient) algorithm to designate which values belong to which experiment and plot them.
4) It is suggested that you use the Plot Editor UI to manipulate the figure to your liking.

4.5.8 Possible Improvements in Programming

1) Let Matlab determine contact. It could also be used to correct for virtual deflection of the free-equilibrium region using a line subtraction.

2) Let Matlab determine how many points to use in the linear fits depending on the number of data points in the FC.
3) Combine programs into one, so it crops and fits one FC at a time, but will completely crop and fit a data set with one script.
4) Create a program that can attempt to fit a sphere to the tip in order to determine tip radius.
5) Fit three-dimensional profile of tip to calculate a unique force model for that particular tip!

4.6 Appendix VI – Nanophysics M.S. Proposal

4.6.1 Objective

The approval of an individually designed B.S./M.S. program in the area of nanoscale physics similar to those offered at other universities, to address the needs of one student, Evan Anderson PH, WPI '09.

4.6.2 Justification

Nanoscience is a relatively new branch of science that has been developing rapidly over the last decade. It is technology pertaining to objects or theory on the scale of one-billionth of a meter; one thousand times smaller than the micro scale. This new technology is of tremendous interest to practically all fields of science, particularly computer and health sciences, because of its tendency to completely renovate the efficiency of a process. For these reasons, many of the prominent universities around the world have begun to offer nanoscience programs including: Rice University, Arizona State University, and Delft University.

Nanophysics is to nanotechnology as physics is to engineering. While engineering focuses on the solutions to common problems, physics takes more care to understand their origin and mechanics. Nanophysics follows the same trend by attempting to explain observations made by nanotechnology. Nanophysics relies heavily on quantum mechanics, statistical mechanics, and solid-state physics, as well as some advanced classical

mechanics. Many nanoscale phenomena can be explained by the aforementioned disciplines of physics.

Since the nanoscience field is relatively new, there are also a large variety of career opportunities. Although an exceptional physics student should be qualified to solve many problems faced in nanoscience, employers are much more likely to choose candidates with direct experience and study of nanoscience; a student of nanophysics or nanoscience would be much more qualified than an ordinary physics student. It is for this reason Mr. Anderson would like to propose a curriculum within WPI's offered classes that fits other prestigious schools' criteria for a nano-related degree. The proposed curriculum will focus on physics slightly more than some other universities (examples given in appendix).

Using GradSchools.com as a search engine, only 39 hits are returned (excluding online courses) for schools world-wide that offer degrees related to nanotechnology or nanoscience. Of these 39 hits, only 13 schools offer degrees specifically dealing with nanoscience—with others suggesting broader programs that may encompass some nanoscience. Some common degree requirements from these 13 schools involve background in: Characterization of Nanomaterials and Nanostructures, Fabrication and Control of Nanomaterials and Nanostructures, and Devices, Systems, and Integration of Nanotechnology.

4.6.3 Proposed B.S/M.S. Curriculum

Table 1- Courses to be Used from WPI's B.S. Program

Course	Course Title	Grade	Credits
PH 522	Thermodynamics and Statistical Mechanics	B	3
PH 3502*	Solid State Physics*	A	3
MA 4451°	Boundary Value Problems°	B	3
MQP	Polymer Brush Force Modeling and Experimentation	A	3
Total Credits			**12**

*Although a 3000-level course, its background is two other 3000-level courses, and it suggests background in a 4000-level course, so it is effectively a 4000-level course.
°This course provides essential mathematical skills for higher level physics courses.

Table 2 – Courses to be Taken Fall 2009- Spring 2010

Course	Course Title	Credits
PH 511	Classical Mechanics	3
PH 514	Quantum Mechanics I	3
PH 599	Master's Thesis	3
MTE 575	Introduction to Nanomaterials and Nanotechnology	3
MTE 594	Electron Microscopy	3
CHE 580	Nanobiotechnology	3
Total Credits		**18**

The primary subject areas required at other universities are easily covered by this proposed program. Again, a common trend for degree requirements was found between other universities: Characterization, Fabrication & Control, and Devices, Systems, and Integration. We also believe a fourth aspect is particularly important for a nanophysics degree, physics at the nanoscale.

4.6.3.1 Characterization

Mr. Anderson has already had some experience with Characterization with PH 2510 Atomic Force Microscopy. His entire Major Qualifying Project involved characterization of bacterial polymers with an atomic force microscope, as will his thesis research. Characterization is also investigated in PH 3502 Solid State Physics with x-ray diffraction and crystallography. MTE 594 Electron Microscopy examines other methods to characterize nanostructures. In addition to learning about all types of electron microscopy in this course, students will be trained to use both a scanning electron microscope and a transmission electron microscope and will be required to conduct their own research. The MTE 575 Introduction to Nanomaterials and Nanotechnology course will also cover some characterization.

4.6.3.2 Fabrication and Control

MTE 575 Introduction to Nanomaterials and Nanotechnology covers some fabrication and control of nanostructures. The course also requires a half-semester of research and lab work in a topic of choice which will provide more experience in this area. Mr. Anderson's MQP, Polymer Brush Force Modeling and Experimentation, also dealt with fabrication and control in the preparation of the experimental samples for atomic force microscopy. A layer of polymers had to be assembled and firmly bound to a glass slide in order to model the polymer brush of a bacterium. This was done using a chemical procedure.

4.6.3.3 Devices, Systems, and Integration

PH 3502 Solid State Physics investigated some devices that rely on nanoscience such as semiconductors and transistors. The course itself essentially implies an investigation of nanoscale systems—as does Quantum Mechanics and Statistical Mechanics. Some universities couple nanosciences with biophysics and nanobiology. These are nano and microscale systems and are the primary focus of CHE 580 Nanobiotechnology. MTE 575 Introduction to Nanomaterials and Nanotechnology also encompasses this entire topic of devices, systems, and integration.

4.6.3.4 Nanophysics

There are several physics courses that can help to make predictions and analyze observations at the nanoscale. Quantum Mechanics is itself a nanophysics course. Solid State Physics is also primarily a study of physics at the nanoscale; it predicts structures and behaviors of solids based on their atomic constituents. Statistical Mechanics is a microscopic physical understanding of the macroscopic observations made by thermodynamics; it accounts for each individual molecule or atom—in this respect, it is also a nanophysics course. Mr. Anderson's MQP also dealt heavily with nanophysics. It was an investigation of a current force model used to describe the interaction between an atomic force microscope tip and a bacterial brush. This exemplifies how classical mechanics and thermodynamics can be applied to nanoscale interactions. Mr. Anderson's master's thesis will be a continuation of his MQP in an attempt to correct the interpretation of a particular parameter in this force model.

4.6.4 Student Background

Mr. Anderson studied Physics as an undergraduate and minored in Nanoscience. The minor was individually designed and proposed originally in October of 2008—it was accepted in early 2009. The courses that earned this minor are shown in the following table.

Table 3 – Courses Taken to Earn Nanoscience Minor

Course	Course Title	Purpose	Grade
CH 1010	Molecularity	Structure of Molecules	B
BB 2920	Genetics	Function of Molecules	B
PH 3401	Quantum Mechanics I	Quantum Properties of Matter	B
PH 3502	Solid State Physics	Atomic Properties of Matter	A
PH 2510	Atomic Force Microscopy	Characterization and Devices	A
THK NANO	Quantum Dot Tracking in Mesenchymal Stem Cells	Interdisciplinary Capstone Experience	A

In addition to his acceptance to WPI's graduate school, Mr. Anderson was offered a Teaching Assistantship with the Physics department to pursue his Master's Degree. He conducted research at Gateway Park over this past summer continuing his MQP and collecting data for use in his master's thesis.

Mr. Anderson started at WPI as an ECE major, but was unsure of what exactly he wanted to specialize in. For this reason, he changed his major to Physics so that he would have time to decide what he wanted to do and have a solid foundation for most other majors

at the same time. Mr. Anderson discovered the direction he wanted to take after taking the class PH2510 Atomic Force Microscopy—he wanted to study Nanoscience. It was for this reason he was driven to pursue the Minor in Nanoscience, and he overloaded in order to do so in his senior year. Mr. Anderson is determined to work in the nanoscience field and is eager to take advantage of any opportunity that will help him do so. A degree in Nanophysics would greatly assist him in his aspiration.

4.6.5 Faculty Committee

Professor (Department)	Research Interests
Nancy A. Burnham (PH)	Scanning probe microscopy, nanomechanics, molecular engineering, and nanotechnology.
Terri A. Camesano (CHE)	Bacterial adhesion and interaction forces, biopolymers, bacterial-natural organic matter interactions, and colloid-polymer interactions..
Jianyu Liang (ME)	Nanofabrication, nanomanufacturing, nano-optoelectronics, nanobioengineering, application of nanomaterial in batteries and power sources, and magnetic nanodots and nanowires for information storage and computing.
Boquan Li (MTE)	Growth and structural characterization of nanostructured materials, Nanomaterials in energy storage and conversion applications, and electron microscopy.

4.6.6 Supplementary Information

The following are some highly respected universities in the world that offer nanoscale programs. Included are the core course requirements and descriptions for the program.

4.6.6.1 Rice University (Houston, TX)

Master of Science – Nanoscale Physics

The coursework in the Professional Master's Program track in Nanoscale Physics involves fundamental quantum theory and its application to practical materials and devices. New courses cover cutting-edge areas such as quantum behavior of nanostructures, quantum nanotechnology, nanoscale imaging, and the fabrication of nanostructures. (Taken from the Nanoscale Physics program website: http://www.profms.rice.edu/nanophysics.aspx?id=162)

Science Core/Cohort Courses	Nanostructures and Nanotechnology Methods of Experimental Physics Characterization and Fabrication at the Nanoscale Methods of Experimental Physics Nanostructures and Nanotechnology II Methods of Experimental Physics II Computational Physics Management in Science and Engineering Professional Master's Seminar Professional Master's Project Science Policy and Ethics
Electives	Introduction to Operations Research Chemical Engineering of Nanostructured Materials Engineering Economics and Management Molecular Spectroscopy and Group Theory Supramolecular Chemistry Nanoscale Chemistry Laser Spectroscopy Imaging at the Nanoscale Nano-optics and Nano-photonics Submicrometer and Nanometer Device Technology Topics in Semiconductor Nanostructures Systems Analysis and Database Design

	International Business Law Production and Operations Management Project Management / Project Finance General Business Law New Venture Creation in Science and Engineering Special Topics: Principles of Nanoscale Mechanics Ultrafast Optical Phenomena

4.6.6.2 Arizona State University (Tempe, AZ)

Professional Science Master's – Nanoscience

Nanoscience is an interdisciplinary subject spanning physics, chemistry and biochemistry, materials and electrical engineering. It concerns the properties of atomic and molecular assemblies (composed of tens, hundreds or thousands of atoms) under an extraordinarily wide range of conditions and geometries, and areas of application. (Taken from ASU Nanoscience P.S.M. website: http://physics.asu.edu/graduate/psm/pos)

Core Courses	Quantum Physics for Nanoscience Professional Seminar Nanoscience and Society Innovation and IP Management
Program Option 1: Nanomaterials and Nanoelectronics	Materials Physics I Topics in Biophysics Electron Microscopy I Materials Physics II Introduction to Nanoscience Surfaces and Thin Films
Program Option 2: Biophysics and Bionanotechnology	Materials Physics I Topics in Biophysics Electron Microscopy I Introduction to Nanoscience Topics in Biophysics II

	Bionanotechnology
Program Option 3: Biophysics, Biochemistry, and Sensors	Topics in Biophysics Introduction to Biosensors Electron Microscopy I Introduction to Nanoscience Electro-analytical Chemistry Bionanotechnology

4.6.6.3 Delft University of Technology (Delft, NL)

Master of Science – Nanoscience and Nanotechnology

(The following was taken from Delft's Nanoscience Program Description website found at http://www.emm-nano.org/Program/programmeDescription.htm)

At the start of the programme the students choose one specialization as their major theme. For this purpose the multidisciplinary field of nanoscale research is subdivided into four major themes: (i) nanotechnology (NT), (ii) nanoscience (NS), (iii) biophysics (BP), (iv) bionanotechnology (BNT).

In the first year the students follow a common program at the KU Leuven, where they are offered a set of introductory courses, non-technical courses, the core courses of the programme, and some electives to prepare them for the specialization in their major.

The Introductory courses (max 12 ects, KU Leuven) introduce the students to disciplines in which they have had no training and which are essential for the core courses in Year 1 and specialization courses in Year 2. For example, a physics student will follow

the introductory course of biochemistry. If a student does not need any introductory course, he/she may choose more elective courses.

The Non-technical course modules (9 ects, KU Leuven) are necessary to impart non-technical qualities to the nanoscientists.

The Core courses (30 ects, KU Leuven) contain the basic knowledge within the four main disciplines: nanotechnology, nanoscience and biochemistry/physics. Every student follows these courses irrespective of her/his specialization.

The Lecture Series on Nanotechnology in Modern Society (3 ects) are organized on a monthly basis by the consortium partners, given by national and international experts on subjects such as "ethics of nanotechnology developments", "opportunities for nanotechnology applications" and "the risks of nanotechnology". Nanoscience and nanotechnology are relatively new subjects, and as such they are accompanied by many uncertainties as to their impact on modern society. We consider this an important aspect of the educational programme. Students need to be aware of the challenges, risks and promises of nanotechnical developments and to contribute to finding answers to open questions. They are expected to attend all of the lectures and to prepare a short report of about 4 pages on one of the lectures of their own choice. The lectures are broadcasted to the four consortium partners.

The Major courses (21-33 ects, Leuven and Delft/Leiden, Chalmers or Dresden) prepare for the master thesis project. They consist of courses with a general character as well of courses highly specialized and directly related to the master thesis research. The

students can choose 6-18 credits elective courses in the first year at the KU Leuven from three course modules (Nanoscience, Nanotechnology, Biophysics/BioNanotechnology). Then in the second year university the students follow 15 credits compulsory courses.

The Broadening (or minor) courses (15 ects, Delft/Leiden, Chalmers or Dresden) allow the students to choose courses from the other themes of the master, which allow them to broaden heir scope beyond the chosen specialization . Students can choose from a large set of courses offered at the second year university.

The Master thesis research project (30 ects, Delft/Leiden, Chalmers or Dresden) is intended to bring the student in close contact with a multinational and multidisciplinary research environment of a research institute in academia or in industry. The student will be assigned a relevant research project and work in close collaboration with PhD students, postdocs and professors. The research project is finalized with a public presentation of a Master's Thesis at the second year university, and is also evaluated by an external examiner at the KU Leuven.

Specializing Courses	Nanotechnology Quantum Electronics and Quantum Optics Advanced Semiconductor Devices Master Thesis
Broadening Courses	Mesoscopic Physics Advanced Quantum Mechanics Quantum Electronics and Quantum Optics Physics of Semiconductor Nanodevices Supramolecular Chemistry Molecular Electronics Advanced Statistical Mechanics

	Polymer Structure and Dynamics Nanostructured Polymers Biophysics Nanotechnology Advanced Solid State Physics Advanced Semiconductor Devices Advanced Materials Surface Science Biomolecular Motors Systems Biology Quantum Optics and Quantum Information Statistical Physics Theory of Condensed Matter Ethics and Engineering Advanced Biophysics In-vivo Biomolecular Interactions Thin Film Matierals Nanoparticulate Materials Quantum Theory Superconductivity Quantum Transport

5. References

1. Boyd, R.D., et al., *Use of the atomic force microscope to determine the effect of substratum surface topography on bacterial adhesion.* Langmuir, 2002. **18**(6): p. 2343-2346.
2. Whitehead, K., et al., *Use of the atomic force microscope to determine the effect of substratum surface topography on the ease of bacterial removal.* Colloids and Surfaces B-Biointerfaces, 2006. **51**(1): p. 44-53.
3. Williams, J.A. and H.R. Le, *Tribology and MEMS.* Journal of Physics D-Applied Physics, 2006. **39**(12): p. R201-R214.
4. Bostrom, M., D.R.M. Williams, and B.W. Ninham, *Specific ion effects: Why DLVO theory fails for biology and colloid systems.* Physical Review Letters, 2001. **8716**(16).
5. LaTorre, C. and B. Bhushan, *Nano tribological characterization of human hair and skin using atomic force microscopy.* Ultramicroscopy, 2005. **105**(1-4): p. 155-175.
6. McMullen, R.L. and S.P. Kelty, *Investigation of human hair fibers using lateral force microscopy.* Scanning, 2001. **23**(5): p. 337-345.
7. Palacio, M.L.B. and B. Bhushan, *Normal and Lateral Force Calibration Techniques for AFM Cantilevers.* Critical Reviews in Solid State and Materials Sciences, 2010. **35**(2): p. 73-104.
8. Munz, M., *Force calibration in lateral force microscopy: a review of the experimental methods.* Journal of Physics D-Applied Physics, 2010. **43**(6).
9. Wright, C.J. and I. Armstrong, *The application of atomic force microscopy force measurements to the characterisation of microbial surfaces.* Surface and Interface Analysis, 2006. **38**(11): p. 1419-1428.
10. Pettersson, T., N. Nordgren, and M. Rutland, *Comparison of different methods to calibrate torsional spring constant and photodetector for atomic force microscopy friction measurements in air and liquid.* Review of Scientific Instruments, 2007. **78**(9): p. -.
11. Anderson, E.V., et al., *Shape-Independent Lateral Force Calibration.* ACS Applied Materials & Interfaces, 2011. **3**(9): p. 3256-3260.
12. Costerton, J.W., P.S. Stewart, and E.P. Greenberg, *Bacterial biofilms: A common cause of persistent infections.* Science, 1999. **284**(5418): p. 1318-1322.
13. Cunningham, A.B., J.E. Lennox, and R.J. Ross. *Biofilms: The Hypertextbook*. 2008 [cited 2008-2009; Available from: www.biofilmbook.com.
14. Rickard, A.H., et al., *Bacterial coaggregation: an integral process in the development of multi-species biofilms.* Trends in Microbiology, 2003. **11**(2): p. 94-100.
15. Ivanov, I.E., et al., *Relating the Physical Properties of Pseudomonas aeruginosa Lipopolysaccharides to Virulence by Atomic Force Microscopy.* Journal of Bacteriology, 2011. **193**(5): p. 1259-1266.
16. Camesano, T.A. and B.E. Logan, *Probing bacterial electrosteric interactions using atomic force microscopy.* Environmental Science & Technology, 2000. **34**(16): p. 3354-3362.

17. Degennes, P.G., *Polymers at an Interface - A Simplified View*. Advances in Colloid and Interface Science, 1987. **27**(3-4): p. 189-209.
18. Butt, H.J., et al., *Steric forces measured with the atomic force microscope at various temperatures*. Langmuir, 1999. **15**(7): p. 2559-2565.
19. Chang, D.P., et al., *Conformational Mechanics, Adsorption, and Normal Force Interactions of Lubricin and Hyaluronic Acid on Model Surfaces*. Langmuir, 2008. **24**: p. 1183-1193.
20. Sokolov, I., et al., *Detection of surface brush on biological cells in vitro with atomic force microscopy*. Applied Physics Letters, 2007. **91**(2).
21. Taylor, E.S. and S.K. Lower, *Thickness and Surface Density of Extracellular Polymers on Acidithiobacillus ferrooxidans*. Applied and Environmental Microbiology, 2008. **74**(1): p. 309-311.
22. Attili, S. and R. Richter, *Combining Colloidal Probe Atomic Force and Reflection Interference Contrast Microscopy to Study the Compressive Mechanics of Hyaluronan Brushes*. Langmuir, 2012. **28**(6): p. 3206-3216.
23. Block, S. and C. Helm, *Conformation of poly(styrene sulfonate) layers physisorbed from high salt solution studied by force measurements on two different length scales*. Journal of Physical Chemistry B, 2008. **112**(31): p. 9318-9327.
24. O'Shea, S.J., M.E. Welland, and T. Rayment, *An atomic force microscope study of grafted polymers on mica*. Langmuir, 1993. **9**(7): p. 1826-1835.
25. Gaboriaud, F., et al., *Surface structure and nanomechanical properties of Shewanella putrefaciens bacteria at two pH values (4 and 10) determined by atomic force microscopy*. Journal of Bacteriology, 2005. **187**(11): p. 3864-3868.
26. Chandraprabha, M., P. Somasundaran, and K. Natarajan, *Modeling and analysis of nanoscale interaction forces between Acidithiobacillus ferrooxidans and AFM tip*. Colloids and Surfaces B-Biointerfaces, 2010. **75**(1): p. 310-318.
27. Lee, C., et al., *Frictional Characteristics of Atomically Thin Sheets*. Science, 2010: p. 76-80.
28. Park, J., et al., *Electronic control of friction in silicon pn junctions*. Science, 2006: p. 186-186.
29. Liley, M., et al., *Friction Anisotropy and Asymmetry of a Compliant Monolayer Induced by a Small Molecular Tilt*. Science, 1998. **280**(5361): p. 273-275.
30. Luan, B. and M. Robbins, *The breakdown of continuum models for mechanical contacts*. Nature, 2005: p. 929-932.
31. Mo, Y., K. Turner, and I. Szlufarska, *Friction laws at the nanoscale*. Nature, 2009: p. 1116-1119.
32. Krautbauer, R., M. Rief, and H.E. Gaub, *Unzipping DNA oligomers*. Nano Letters, 2003. **3**(4): p. 493-496.
33. Vezenov, D.V., et al., *Force titrations and ionization state sensitive imaging of functional groups in aqueous solutions by chemical force microscopy*. Journal of the American Chemical Society, 1997. **119**(8): p. 2006-2015.
34. Brewer, N. and G. Leggett, *Chemical force microscopy of mixed self-assembled monolayers of alkanethiols on gold: Evidence for phase separation*. Langmuir, 2004: p. 4109-4115.

35. Tambe, N.S. and B. Bhushan, *Micro/nanotribological characterization of PDMS and PMMA used for BioMEMS/NEMS applications.* Ultramicroscopy, 2005. **105**(1-4): p. 238-247.
36. Cannara, R.J., M. Eglin, and R.W. Carpick, *Lateral force calibration in atomic force microscopy: A new lateral force calibration method and general guidelines for optimization.* Review of Scientific Instruments, 2006. **77**(5).
37. Li, Q., K.S. Kim, and A. Rydberg, *Lateral force calibration of an atomic force microscope with a diamagnetic levitation spring system.* Review of Scientific Instruments, 2006. **77**(6).
38. Varenberg, M., I. Etsion, and G. Halperin, *An improved wedge calibration method for lateral force in atomic force microscopy.* Review of Scientific Instruments, 2003. **74**(7): p. 3362-3367.
39. Asay, D.B. and S.H. Kim, *Direct force balance method for atomic force microscopy lateral force calibration.* Review of Scientific Instruments, 2006. **77**(4).
40. Jeon, S., Y. Braiman, and T. Thundat, *Torsional spring constant obtained for an atomic force microscope cantilever.* Applied Physics Letters, 2004. **84**(10): p. 1795-1797.
41. Feiler, A., P. Attard, and I. Larson, *Calibration of the torsional spring constant and the lateral photodiode response of frictional force microscopes.* Review of Scientific Instruments, 2000. **71**(7): p. 2746-2750.
42. Reitsma, M.G., *Lateral force microscope calibration using a modified atomic force microscope cantilever.* Review of Scientific Instruments, 2007. **78**(10).
43. Ecke, S., et al., *Measuring normal and friction forces acting on individual fine particles.* Review of Scientific Instruments, 2001. **72**(11): p. 4164-4170.
44. Green, C.P., et al., *Normal and torsional spring constants of atomic force microscope cantilevers.* Review of Scientific Instruments, 2004. **75**(6): p. 1988-1996.
45. Ogletree, D.F., R.W. Carpick, and M. Salmeron, *Calibration of frictional forces in atomic force microscopy.* Review of Scientific Instruments, 1996. **67**(9): p. 3298-3306.
46. Stiernstedt, J., M.W. Rutland, and P. Attard, *A novel technique for the in situ calibration and measurement of friction with the atomic force microscope.* Review of Scientific Instruments, 2005. **76**(8).
47. Ruan, J.A. and B. Bhushan, *Atomic-Scale Friction Measurements Using Friction Force Microscopy. 1. General Principles and New Measurement Techniques.* Journal of Tribology-Transactions of the Asme, 1994. **116**(2): p. 378-388.
48. Bennewitz, R., *Friction force microscopy.* Materials Today, 2005. **8**(5): p. 42-48.
49. Matei, G., et al., *Precision and accuracy of thermal calibration of atomic force microscopy cantilevers.* Review of Scientific Instruments, 2006.
50. Liu, J., et al., *Preventing Nanoscale Wear of Atomic Force Microscopy Tips Through the Use of Monolithic Ultrananocrystalline Diamond Probes.* Small, 2010: p. 1140-1149.
51. Abu-Lail, N.I. and T.A. Camesano, *Role of Lipopolysaccharides in the Adhesion, Retention, and Transport of Escherichia coli JM109.* Environmental Science & Technology, 2003. **37**(10): p. 2173-2183.

52. Camesano, T.A. and N.I. Abu-Lail, *Heterogeneity in Bacterial Surface Polysaccharides, Probed on a Single-Molecule Basis.* Biomacromolecules, 2002. **3**(4): p. 661-667.